# Analysing stress field conditions of the Colima Volcanic Complex (Mexico) by integrating FEM simulations and geological data

Silvia Massaro[1,2], Roberto Sulpizio[1,2,3], Gianluca Norini[2], Gianluca Groppelli[2], Antonio Costa[1], Lucia Capra[4], Giacomo Lo Zupone[5], Michele Porfido[6], Andrea Gabrieli[7]

[1]Istituto Nazionale di Geofisica e Vulcanologia, Via D. Creti 12, 40128, Bologna, Italy
[2]Istituto di Geologia Ambientale e Geoingegneria, Consiglio Nazionale delle Ricerche, Via M. Bianco 9, 20131, Milan, Italy
[3]Dipartimento di Scienze della Terra e Geoambientali, Via E. Orabona 4, 70125, Bari, Italy
[4]Centro de Geociencias, Universidad Nacional Autonoma de Mexico, Queretaro, Mexico
[5]Institute of New Energy and Low-carbon Technology, Sichuan University, Chengdu, PRC
[6]Alumni Mathematica, Dipartimento di Matematica, Via E. Orabona 4, 70125, Bari, Italy
[7]Hawai'i Institute of Geophysics and Planetology, 1680 E-W Road, Honolulu, Hawai'i 96922, USA

*Corresponding author: Silvia Massaro (silvia.massaro@ingv.it).

**Abstract**

In recent decades, Finite Element Modelling (FEM) has become a very popular tool in volcanological studies, and has been used to describe even complex system geometries, accounting for multiple reservoirs, topography and heterogeneous distribution of host rock mechanical properties. In spite of this, the influence of geological information on numerical simulations is still poorly considered. In this work, a 2D Finite Element Modelling FEM of the Colima Volcanic Complex (Mexico) is provided by using the LInear Static Analysis (LISA) software, in order to investigate the stress field conditions at increasing detail of geological data. By integrating the published geophysical, volcanological and petrological data, we modelled the stress field considering either one or two magma chambers connected to the surface via dykes or isolated (not connected) in the elastic host rocks (considered homogeneous and non homogeneous). We also introduced tectonic disturbance, considering the effects of direct faults bordering the Colima Rift and imposing an extensional far- field stress of 5 MPa. We raun the model using gravity in the calculations. Our results suggest that an appropriate set of geological data is of pivotal importance for obtaining reliable numerical outputs, which can be considered as a proxy for natural systems.  Beside and beyond the importance of geological data in FEM simulations, the model runs using the complex feeding system geometry and tectonics show how the present-day Colima volcanic system can be considered in equilibrium from aby stress state point of view, in agreement with the long- lasting open conduit dynamics that have lasteds since 1913.

## 1 Introduction

Magmatism and tectonism are strongly related to regional and local stress fields, affecting both the orientation of faults and the location of volcanic vents (Geyer et al., 2016). The stress field around a magmatic source originates from three main contributions: (1) the background stress, composed of a vertical gravitational load, a lateral horizontal load (lithostatic confinement) and tectonic regime; (2) the stress field caused by the loading of the volcano edifice; and, (3) the stress field generated by the magmatic pressure (e.g. Martíí and Geyer, 2009; Currenti and Williams et al., 2014). In recent years, a large number of semi-analytical and numerical methods have been proposed tfor the solveution theof stress field state of natural systems (e.g. Cayol and Cornet, 1998; Simms and Garven, 2004; Manconi et al., 2007; Long and Grosfils, 2009; Currenti et al., 2010; Currenti and Williams et al., 2014; Zehner et al., 2015), taking into account the static elastic deformation in a multi-layered half-space (e.g. Dieterich and Decker, 1975; Bonafede et al., 2002; Wang et al., 2003; Gudmundsson and Brenner, 2004; Pritchard and Simons, 2004; Zhao et al., 2004; Pritchard and Simons, 2004; Gottsmann et al., 2006; Geyer and Gottsmann, 2010; Zhong et al., 2019). Following the successful application in mechanical engineering, fluid dynamics and thermodynamics (e.g., Gutiérrez and Parada, 2010; Gelman et al., 2013), the use of Finite Element Modellingethod (FEM) has been introduced extensively introduced in volcanology, in order to investigate the effects of topography, lithologic heterogeneities, tectonic stresses and the gravity field on the stress state of volcanic systems (e.g. Fujita et al., 2013; Bunney, 2014; Carcho and Gàlan del Sastre, 2014; Hickey et al., 2015; Bunney, 2014; Ronchin et al., 2015; Hickey et al., 2015; Cabaniss et al., 2019; Rivalta et al., 2019).

There are several examples of the use of FEM for volcanic systemshas several examples, which spanning from the influence of layered materials on the surface deformation process during volcanic inflation (e.g. Darwin volcano, Galapagos Islands; Manconi et al., 2007; Albino et al., 2010) to processes affecting chamber rupture (e.g. Grosfils, 2007; Long and Grosfils, 2009).

The local stress around a volcanic feeding system depends on the geometry of the magma plumbing system, including the chamber(s) and dykes forming it, and on the mechanical properties of the host rock around it (e.g. Martí and Geyer, 2009), and especially on changes in Young modulus (e.g. Gudmundsson et al., 2011; Jeanne et al., 2017; Heap et al., 2020). For instance, limestone, lava flows, welded pyroclastic deposits and subvolcanic rocks can be very stiff (high Young modulus; ca. 1.7–27 GPa for limestones, Touloukian, 1981; ca. 5.4 GPa for volcanic rocks, Heap et al., 2020), but young and non-welded pyroclastic units may be very soft (low Young modulus; ca. 1.7 – 3.1 GPa, Margottini et al., 2013). Therefore, the local stress may change abruptly change from one layer to another (e.g., Gudmundsson, 2006). Irrespective of the scope of the numerical investigation, the importance of applying accurate physical constraints to FEM hwas already been discussed in many studies (e.g., Folch et al., 2000; Fernandez et al., 2001; Newman et al., 2001; Fernandez et al., 2001; Currenti et al., 2010; Geshi et al., 2012). However, in the last decade, few investigations have been carried out to assess the influence of the amount and quality of geological data ointo FEM computations (Kinvig et al., 2009; Norini et al., 2010, 2019; Cianetti et al., 2012; Ronchin et al., 2013; Chaput et al., 2014; Norini et al., 2019). To bridge this gap, in this work we used the LInear Static Analysis (LISA) software (version 8.0; www.lisafea.com) to study the subsurface stress field state inat the Colima Volcanic Complex (CVC, Mexico) at increasing geological detail.

The CVC area is a good candidate for testing the response of FEM software against different geological conditions, being constituted by a large volcanic complex (Lungarini et al., 2005) within a tectonic graben filled with volcaniclastic material (Fig. 1a; Norini et al., 2010, 2019). The FEM was run starting from simple homogeneous vs stratified lithology of the subsurface, and in successively more detail by the addition of single and double magma chambers, feeder dykes, faults and extensional far-field tectonic stress (Fig. 1b).

## 2 The Colima Volcanic Complex (Mexico)

### *2.1 Geological framework*

The Pleistocene–Holocene CVC is one of the most prominent volcanic edifices within the Trans-Mexican Volcanic Belt (TMVB) (Macías et al., 2006; Capra et al., 2016; Norini et al., 2019; Fig. 1a). In this area, the Rivera microplate and the Cocos plate subduct beneath the North America plate along the Middle American Trench (Stock and Lee, 1994), forming a triple junction that delimits the tectonic units known as the Jalisco Block (JB) and the Michoacán Block (MB) (Luhr et al., 1985; Allan, 1986; Rosas-Elguera et al., 1996, 1997; Ferrari and Rosas-Elguera, 1999; Rosas-Elguera et al., 2003; Frey et al., 2007). The three rifts of this system are the Tepic–Zacoalco Rift (TZR), Chapala–Tula Rift (CTR) and Colima Rift (CR). The still-active NS-trending CR was formed during a rifting phase which occurred after the Late Cretaceous–Paleogene compressive and transpressive phase (Allan, 1986; Serpa et al., 1992; Bandy et al., 1995; Cortés et al., 2010). While opening, the CR was gradually filled with Pliocene–Quaternary lacustrine sediments, alluvium and colluvium (e.g. Allan, 1986; Allan et al., 1991; Norini et al., 2010). The geometry, kinematics and dynamics of the CR have been studied on the basis of field, seismic and geodetic data, mainly collected in its northern and central sectors (see Fig. 1 in Norini et al., 2010).

The magnitude of vertical displacement of the northern and central sectors is ca. 2.5 km by adding the topographic relief of the bounding fault scarps (1.5–1.6 km) to the calculated sediment depth (Allan, 1985; Serpa et al., 1992). Field data and focal mechanism solutions are consistent with a direction of opening of the northern and central sectors oriented from E–W to NW–SE, with mainly normal and minor right-lateral displacements of the bounding faults (Barrier et al., 1990; Suárez et al., 1994; Rosas-Elguera et al., 1996; Garduño-Monroy et al., 1998; Norini et al., 2010, 2019). In contrast to field and seismic evidence of long-term slightly dextral oblique extension, recent GPS geodetic measurements suggest a possible left oblique extension of the CR (Selvans et al., 2011). In both cases, the stress regime is extensional with an E–W orientation of the minimum horizontal stress in the CVC basement (Barrier et al., 1990; Suárez et al., 1994; Rosas-Elguera et al., 1996; Norini et al., 2010; Selvans et al., 2011; Norini et al., 2019).

The CVC stands within the central sector of the CR, on top of Cretaceous limestone, Late Miocene–Pleistocene volcanic rocks and Pliocene–Holocene lacustrine sediments, alluvium and colluvium (Allan, 1985, 1986, 1991; Cortés, 2005; Norini et al., 2010; Escudero and Bandy, 2017). It is formed by three andesitic stratovolcanoes: Cantaro (2900 m a.s.l.), Nevado de Colima (4255 m a.s.l.) and, in the southern part, the youngest and active Volcàn de Colima (3763 m a.s.l.) (Norini et al., 2019 and reference therein; Fig. 1a).

### *2.2 Eruptive activity*

The eruptive history of the CVC started in the northeast area with the formation of Cantaro volcano at ca. 1–1.5 Ma followed by Nevado de Colima at ca. 0.53 Ma, which is composed of voluminous andesitic lava domes and deposits associated with caldera-forming eruptions and partial sector collapses (Robin et al., 1987; Roverato et al., 2011; Roverato and Capra, 2013; Cortés et al., 2019). The youngest – Volcàn de Colima – comprises the Paleofuego edifice, which suffered several sector collapses that formed a horseshoe-shaped depression where the new active cone (also known as Volcàn de Fuego) grew up. Its activity was characterized by dome growths and collapses, extrusion of lava flows, and Vulcanian and occasionally sub-Plinian explosive eruptions (Saucedo et al., 2010; Massaro et al., 2018, 2019).

### *2.3 The CVC plumbing system*

Seismic tomography (Spica et al., 2017) highlights a 15 km-deep low velocity body (LVB), which was interpreted as a deep magma reservoir. It is confined within the CR, suggesting a structural control of the normal fault system on it (Spica et al., 2014). The LVB has an extent of ca. 55 km × ×30 km in the N–-S and E–-W directions, respectively, showing an averaged thickness < 8 km. Escudero and Bandy (2017) obtained a higher- resolution tomographic image of the CVC subsurface area, showing that the most active magma generation zone is now under the Fuego de Colima edifice. The ambient seismic noise tomographic study of Spica et al. (2014) indicates a shallow magma chamber above ca. 7 km depth, in agreement with petrological studies (Medina-Martinez et al., 1996; Luhr, 2002; Zobin et al., 2002; López-Loera et al., 2011; Reubi et al., 2013, 2019; Macíasìas et al., 2017; Reubi et al., 2019). Cabrera-Gutiérrez and Espíndola (2010) suggested the shallow active magma storage has a volume of ca. . 30 30 $km^3$. It is connected to the surface by conduits, whose path is facilitated by the presence of the CR fault zone, which provide a natural pathway for fluids (e.g., Allan, 1986; Norini et al., 2010, 2019). The arrangement of dykes and the alignment of the volcanic centres of the CVC suggest that the dykes swarms draining the magma chambers developed along the NNE–-SSW-trending, steep, eastward- dipping normal fault exposed on the northern CVC flank (Norini et al., 2010, 2019).

Massaro et al. (2018) provided a first-order geometrical reconstruction of the Fuego de Colima feeding system during the 1913 sub-Plinian eruption, using volcanological data (Saucedo et al., 2010; Bonasia et al., 2011; Saucedo et al., 2011) as inputs and constraints for numerical simulations. Results showed good matches for a hybrid configuration of the shallow conduit feeding system composed of a ca. 5500 5500 m- long, 200–-2000 m- wide, and 40 m width dyke passing into a shallower (500 m long, 40 m diameter) cylindrical conduit. The shallow magma chamber top was set at 6 km of depth, and dyke-–cylinder transition at 500 m below the summit as inferred from geophysical data (Salzer et al., 2014; Aràmbula et al., 2018).

## 3 Methods

In this study, we used the commercial 8.0 version of LISA (www.lisafea.com), a general-purpose Finite Element Analysis (FEA) software program developed in the 1990s and based on the formulations proposed by Rao (1989), and successively integrated from other sources (Bathe, 1990; Michaeli, 1991; Schwarz, 1991; Babuska et al., 1995). Despite LISA originally being used for structural analysis (Rao, 1989, 2013), it successfully predicts the stress–strain behaviour of rock masses in elastic models, in particular the deformation mechanisms even in layered rock masses (Gabrieli et al., 2015).

### *3.1 Modelling approach*

The stress field of the CVC plumbing system is simulated considering an E–W cross-section, parallel to the extension associated with the active CR (Norini et al., 2010, 2019) as shown in Figure 1a–b (a–a').

Since the extent of the CVC magma chambers in the NNE–SSW direction is typically much longer than the dimensions of the E–W cross-section (Spica et al., 2017), 2D solutions of either numerical or analytical models describing E–W elongated magma chambers in the crust can be reasonably adopted (Jaeger et al., 2009; Costa et al., 2011). A topographic profile and 2D plane along the chosen E–W cross-section of the CVC area was obtained in ESRI ArcGIS from a Digital Elevation Model (DEM, resolution 50 m; Instituto Nacional de Estadística y Geografía – INEGI https://en.www.inegi.org.mx/) and imported into Autodesk Auto-Cad R13 using a third-degree spline approximation. The IGES file was then imported into LISA for the mesh discretization.

The investigated domain extends 60 × 30 km in an *x*–*z* Cartesian Coordinate System with three- and four-node finite element discretization (Table 1). Zero normal displacements are assigned at the bottom and the lateral boundaries, while the upper boundary represents the free-stress ground surface (Fig. 1c).

The FEM is carried out using a plane strain approximation, implying that the deformation in the third direction is assumed to be negligible.

As reported by Zehner et al. (2015), FEM of geological structures requires accurate discretization of the computational domain. It follows that the unstructured tetrahedral meshes have to fulfil the following requirements: i) sufficient mesh quality: the tetrahedrons should not be too acute-angled, since numerical instabilities can occur; ii) incorporation of geometry for defining boundary conditions and constraints; and iii) local adaption, which is a refinement of the mesh in the vicinity of physical sources in order to avoid numerical errors during the simulation. In this work, we adopted a mesh composed of 4660 plane continuum elements, which have been refined in the regions of higher gradients (i.e. near the contours of the magmatic feeding system).

In our simulations, the extent of the rock layers (Table 2) refers to that used by Norini et al. (2010, 2019). The configuration of the CVC feeding system (i.e. depth, shape and dimensions of the magma chambers and feeder dykes) derives from the literature (Spica et al., 2014, 2017; Massaro et al., 2018, 2019) and is simplified in Figure 1d. In particular, magma chambers and dykes are considered as pressurized finite-size bodies in an elastic crustal segment, acting as fluid-filled holes. The boundary condition (pressurization) is provided by applying internal forces that act on the walls. This approach has been used extensively in several analytical and numerical models that treat magma reservoirs as internally pressurized ellipsoidal cavities within an elastic half-space, in order to gain insight into the behaviour of magma plumbing systems (Pinel and Jaupart, 2004; Gudmundsson, 2006; Grosfils, 2007; Andrew and Gudmundsson, 2008; Hautmann et al., 2013; Currenti and Williams, 2014; Zhong et al., 2019).

Previously published studies indicate that differences between, and problems with, elastic models derive principally from the key role played by gravity (e.g. Lister and Kerr, 1991; Watanabe et al., 2002; Gerbault, 2012; Albino et al., 2018Gerbault, 2012; Lister and Kerr, 1991; Watanabe et al., 2002). Some authors have argued ondiscussed whether or not it is appropriate or not to account for the gravity body force in models of volcanic systems (e.g. Currenti and Williams, 2014; Grosfils et al., 2015).

When the gravitational loading is not included in the model, the volcanic deformation results from a change with respect to a stage previously at equilibrium (e.g. Gerbault et al., 2018). In this work, we carried out simulations considering the effect of the gravitational loading in the host rock, implemented via body forces. The model initial condition has a pre-assigned lithostatic stress, whose computation, in the presence of topographical and material heterogeneities, is not trivial because it requires application ofying the gravity load, preserving the original non-t deformed geometry of the mesh (Cianetti et al., 2012). Since Due to the presence of a lithostatic stress field, the load applied at the reservoir boundaries represents a superposition of the magmatic pressure and lithostatic component. We define here the magmatic pressure as either excess pressure (□$P_e$, magmatic minus lithostatic pressure but below the tensile strength of wall rocks) or over pressure (or driving pressure □$P_o$, which is the magmatic pressure exceeding the tensile strength of wall rocks; Gudmundsson, 2012). The first pertains to the FEMs using isolated magma chambers (single or double), while the second is used for models with connected magma chambers (with conduit/feeding system).

We also took into account the effect of the existing faults of the CR system even though LISA cannot include a frictional law to represent the fault movement (i.e. Chaput et al., 2014). As reported byin Jeanne et al. (2017 and reference therein), the damage induced by faults increases from the host rocks to the fault core, implying the a reduction in the effective elastic moduli. In this light, we represented the faults bordering the CR as two damage zones (ca. 70° of inclination, ca. 1 km thick, and down to 10 km of depth) showing reduced elastic properties with respect to the surrounding host rocks.

To take into account the effect of the far-field extensional regime, we applied a uniform stress of 5 MPa to the lateral boundaries of the domain (as reported by Martí and Geyer, 2009).

Considering the E–W cross-section (a–a'; Fig. 1a), we provided six domain configurations: i) a '“*homogeneous lithology model*”' in which the volcanic domain is only composed of andesite rocks; ii) a '“*non-t homogeneous lithology model*”' where different geological units are considered; iii) a '“*single magma chamber model*”' composed of a not homogeneous lithology and a 15 km-deep magma chamber with non-homogeneous lithology; iv) a '“*dual magma chamber model*”' composed of a nont

-homogeneous and 6 km- and 15 km-deep magma chambers; v) a ‘“*conduit feeding system model*”’ composed of non-t homogeneous *lithology,* 6 km- and 15 km-deep magma chambers connected through a deep dyke evolving into a shallow conduit near the surface; vi) ) an ‘“*extensional model*”’, with a 5 MPa horizontal extensional stress (far field); and, vii) a ‘“*faulted model*”’, in which are also added two damaged zones mimicking the CR faults (local stress) are also added (Fig. 1b).

The number of nodes is set at 4426 for the only substratum and single magma chamber models, at 4161 for the dual magma chamber model and at 3737 for the conduit feeding system and faulted models.

It is important to note that simulation outputs are shown using different colour scales. Although such a choice may make  difficult visual comparison of the different runs difficult, it preserves the necessary details of stress distribution, which would have been lost using a common colour scale.

Finally, in the following we refer to $\sigma_1$ as the greatest compressive stress and $\sigma_3$ as the least compressive stress.

## 4 Geological data

### *4.1 Stratigraphy and rock mechanics*

Four units forming the CVC system are defined from the available geological data (Table 2): i) basement (Unit B): Cretaceous limestones and intrusive rocks forming the bed-rock underlying the CVC; ii) graben fill deposits (Unit GF): Quaternary alluvial, colluvial, and lacustrine deposits filling the graben; iii) Fuego de Colima deposits (Unit FC): andesitic lavas and pyroclastic deposits forming the Paleofuego-–Fuego de Colima edifices; and iv) Volcaniclastic deposits (Unit VD): volcaniclastic deposits covering the southern flank of the CVC (e.g. Cortés et al., 2010; Norini et al., 2010, 2019).

We assumed constant mechanical characteristics within each unit using the typical rock mass properties of density ($\varrho$), Young modulus (E) and Poisson ratio ($\nu$) (Table 2). The rock masses are considered dry, in order for (eventual) pore pressure to be neglected. Only for Unit GF was a higher value for the Poisson ratio used close to the surface in order to mimic the high water content in the graben sediments. The maximum thickness of the graben fill (about 1 km) is assumed from the literature (Allan, 1985; Serpa et al., 1992; Norini et al., 2010, 2019). For Units B and GF, rock mass proprieties are derived from Hoek and Brown (1997) and Marinos and Hoek (2000), while for volcanic materials (units FC and VD; Table 2) they are estimated according to the approach proposed by Del Potro and Hürlimann (2008). In order to describe the effects of the CR faults on stress field distribution, the mechanical properties are locally degraded in proximity to the faults themselves.

*4.2 Geometry of the plumbing system*

In our 2D model, we assume the CVC is composed of two magma chambers connected by dykes and to the surface by a conduit (Fig. 1d). The shape of the magma chambers and dykes is represented by elliptical cross-sections with the major axis *(2a)* and minor axis *(2b) axes*.

Generally, magma chambers have a sill-like shape that is often imaged in seismic studies of volcanoes and rift zones (Macdonald, 1982; Sinton and Detrick, 1992; Mutter et al., 1995; MacLeod and Yaouancq, 2000; Singh et al., 2006; Canales et al., 2009). Most of them are not totally molten but rather a mixture of melt and crystal mush (i.e. Parfitt and Wilson, 2008). Various estimates have been made to infer the actual amount of melt in a magmatic body, showing that it is only ca. 10% of the total chamber volume (Gudmundsson et al., 2012 and reference therein).

After Spica et al. (2017), the 15 km-deep LVB is ca. 7000 $km^3$; therefore, if we assume the melt as 10% melt, the deep magma chamber volume would be ca. 700 $km^3$. Simplifying this volume in an elliptical sill-like geometry, the magma chamber dimensions (i.e. $2a$, $2b$ and $2c$ axes) have to be scaled according to the LVB (55 × 30 × 8 km; Spica et al., 2017) using $2a$ = 14 km, $2b$ = 3.6 km and $2c$ = 26 km, $2c$ being elongated in an NW–SE direction. For the shallow part of the feeder system, we have no detailed geophysical constraints. However, Massaro et al. (2019) reproduced through numerical modelling the nonlinear cyclic eruptive activity at Fuego de Colima in the last 20 years, using a shallow magma chamber volume in the range of 20–50 km$^3$, according to the estimation of Cabrera-Gutiérrez and Espíndolaindola (2010). Here we assume a volume of 30 km$^3$, using $2a$ = 3.5 km, $2b$ = 2 km and $2c$ = 8 km as the dimensions of the shallow magma chamber.

Numerous theoretical and field studies have established that host rock stresses dictate the magma pathways (e.g. Gudmundsson, 2011; Maccaferri et al., 2011, 2011). During ascent to the surface, the dykes align themselves with the most energy-efficient orientation, which is roughly perpendicular to the least compressive stress (e.g. Gonnermann and Taisne, 2015; Rivalta et al., 2019), providing the magma driving pressure remains small compared to the deviatoric stress (Pinel et al., 2017; Maccaferri et al., 2019). This behaviour, however, can be modulated in the presence of significant variations in the fracture toughness of the surrounding rock due to stratification (Maccaferri et al., 2010) or to old and inactive fracture systems (Norini et al., 2019).

Although for oblate magma chambers the propagation of dykes is most probable from the tip areas, in our simulations the orientation of dykes is assumed to be vertical, because of the preferential pathways represented by the CR fault planes (Spica et al., 2017).

We set the dimensions of the feeder dykes in agreement with Massaro et al. (2018): deep dyke $2ad$ = 2 km; shallow dyke $2a$ varies from 1 km at the bottom to 500 m in the upper part of the volcano; width of both deep and shallow dykes $2bd$ = $2b$ = 100 m (Fig. 1d).

It is worth noting that it is outside the scope of this work to provide the conditions for rupture of the magma chamber, LISA accounting only for the elastic regime. For these reasons, we fixed $\Delta P_e$ and $\Delta P_o$ (for isolated and connected magma chamber models, respectively) in the range of 10- –20 MPa for the 15 km-deep chamber, and 5 MPa for the 6 km-deep one. For the dykes and conduit, $\Delta P_o$ is set to 10 MPa in the deeper dyke and 5 MPa in the shallower one, while in the upper 500 m of conduit it is 0.4 MPa.

## Results

In this section, we report the sensitivity analysis carried out to quantify approximation of the Young modulus variation on FEM outputs, and description of the model outputs when adding complexity to the input geological/geophysical data.

*5.1 Sensitivity analysis of Young modulus*

Using the single magma chamber model as a reference case, we quantified the influence of Young modulus variation in each geological unit. Taking into account the mechanical properties of rocks (Table 2) as reference values, we compared the stress state of the computational domain on changing Young modulus by (±) one order of magnitude. This sensitivity analysis, although incomplete, may lead to raised awareness on the selection of input data when running an FEM. The sensitivity analysis was carried out on a reduced simulation domain (the *x*-axis was set to 35 km) in order to diminish the influence of binding effects along the domain borders.

We applied the Euclidean norm (L2) method to illustrate the results. The L2 norm applied on a vector space $x$ (having components $i$ = 1, ... $n$) is strongly related to the Euclidean distance from its origin, and is equal to:

$$||x||2 = \sqrt{\sum_i^n xi^2} \tag{1}$$

In our case, the vector space $x$ is composed of all nodes of the computational domain (Table 1). We defined $xref$, the vector containing the results for the maximum and minimum principal stress, when using the selected values of material properties (Table 1) and $x(-)$ and $x(+)$, the vectors on varying the Young modulus by one order of magnitude in each unit.

In Figure 2 are reported the global relative variations in L2 of $\sigma_1$ and $\sigma_3$ caused by the variation of Young modulus in each unit, for each model configuration (i.e. non-homogeneous lithology, single magma chamber, dual magma chamber and dual magma chamber with conduits models) as follows:

$$\|x\|_{2(-)} = \|x_{ref} - x_{(-)}\|_2 \;/\; \|x_{ref}\|_2 \qquad (2)$$

$$\|x\|_{2(+)} = \|x_{ref} - x_{(+)}\|_2 \;/\; \|x_{ref}\|_2 \qquad (3)$$

All the models show variability of less than 15%, with a few exceptions within Unit B that have variability of over 30% (Fig. 2). In this light, the spatial distribution of the major variations seems not to significantly affect the final stress distributions, because: i) they are located near the mesh borders (Fig. 3a and b); and ii) when not at the mesh borders, the variations are limited to a few % (Fig. 3c and d). It means that a one order of magnitude variation in Young modulus produces variation in FEM outputs distributed over a large domain, and the change affecting the single nodes is limited to a few %.

*5.2 Homogeneous and non-homogeneous lithology*

In Figure 4 we report $\sigma_1$ and $\sigma_3$ stresses for gravity-loaded models with homogeneous lithology composed of only andesitic lavas (Fig. 4a) and non-homogeneous lithology composed of carbonates (Unit B) and alluvional, volcaniclastic and pyroclastic deposits (Units GF and VD; Fig. 4b). It is important to stress that the *x*–*z* zero displacement assigned at the bottom and at the lateral boundaries of the domain created substantial artefacts in the results (i.e. curved patterns of stress), especially considering $\sigma_3$ (Fig. 4, panels i and ii) where the boundary effect on the *x*-axis is amplified by the presence of the upper free surface. It follows that the only unperturbed area extends ca. 30 km horizontally and ca. 15 km vertically (within the blue contour in Fig. 4). It is worth noting that the homogeneous and non-homogeneous models show quite similar stress patterns results (Fig. 4).

*5.3 Gravitational modelling using inferred feeding system geometry*

In Figures 5 and 6 we show three cross-section profiles describing the feeding system starting from a single magma chamber to two chambers, then adding the conduits and, finally, considering the full complexity by adding the effects of far-field stress and CR faults. Figure 5a describes $\sigma_3$ (panel i) and $\sigma_1$ (panel ii) stress distribution for the single magma chamber model and $\Delta P_e = 10$ MPa. No significant differences in the magnitude and pattern of stresses are visible using $\Delta P_e = 20$ MPa (Appendix 1a).

The addition of the shallow magma chamber significantly changes the values and pattern of both $\sigma_3$ and $\sigma_1$ (Fig. 5b). In particular, $\sigma_3$ and $\sigma_1$ stresses describe a typical inflation pattern produced by excess pressure in the magma chamber(s) (Anderson, 1936; Gudmundsson, 2006, 2012), producing well-defined stress arches of $\sigma_3$ (red dotted lines in Fig. 5bi) and divergent strong gradients of $\sigma_1$ around the deep magma chamber (Fig. 5bii). Very slight differences in the magnitude and pattern of stresses appear when using $\Delta P_o = 10$ MPa (Fig. 5b) or 20 MPa (Appendix 1b).

Looking at Figure 6, it is evident how insertion of the conduits in the CVC feeding system dramatically changes the stress distribution, with the disappearance of the stress arch and a nearly constant stress in the computational domain except around the deep magma chamber tips.

*5.4 Application of an extensional stress field*

In order to explore the influence of extensional far-field stress on stress patterns (Fig. 1a), we ran simulations applying 5 MPa stress (typical low value for rift zones; Turcotte and Schubert, 2002; Moeck et al., 2009; Maccaferri et al., 2014; Sulpizio and Massaro, 2017) along the lateral boundaries of the computational domain (Fig. 7).

In the case of a single magma chamber ($\Delta P_e = 10$ MPa; Fig. 7, panels i and- ii), the addition of the far-field stress reduces the confinement effect due to the no displacement condition imposed along the *x*–*z* directions (plane strain approximation). When considering the double magma chamber configuration ($\Delta P_o = 10$ MPa in the deep chamber and $\Delta P_o = 5$ MPa in the shallower one), the presence of the far-field stress produces slight changes in stress magnitude and pattern for both $\sigma_3$ and $\sigma_1$ (Fig. 7, panels iii and iv) with respect to Figure 5b. Very similar effects appears ion the complete feeding system configuration model (Fig. 7, panels v and -vi). Also, in this case using $\Delta Po$ = 20 MPa in the deep magma chamber does not significantly affect the model outputs (Appendix 2).

*5.5 Faults bordering the Colima Rift*

The effect of faults bordering the CR on the final feeding system configuration is simulated through two damage zones by degrading their elastic properties. Adding these elements does not significantly alter the stress distribution observed in Figures 7v and 7vi, but only provides a slight reduction in both $\sigma_1$ and $\sigma_3$ intensities around their edges (Figs. 7vii and 7viii). The different distance of the two damage zones from the feeding system produces a small asymmetry in both $\sigma_1$ and $\sigma_3$ patterns with respect to simulations without damage zones, especially near the deep magma chamber (Figs. 7v–viii).

## 6 Discussion

*6.1 FEM analysis at increasing geological detail*

This study highlights some important features of crustal stress distribution on changing the geological and geophysical constraints as input conditions (Spica et al., 2014, 2017; Massaro et al., 2018). Although the results have to be considered as a first-order approximation, the changes in stress distribution are appreciable and useful for a better understanding of the limitations and advantages of FEM.

Under the assumptions of plane strain and gravitational loading, the use of homogeneous or non-homogeneous lithology provides negligible effects in stress intensity and pattern (Fig. 4). This is likely due to the limited thickness of the shallow units (Units FC, VD and, GF; Table 2) in the simulated domain, which the results of which are dominated by Unit B (Table 2). However, this does not mean that the influence of the upper units may be still negligible using smaller scales of the simulated domain. Analysing the single magma chamber model outputs, it emerges how $\Delta Pe_e$ limits the effects of gravitational loading. On the contrary, the dual magma chamber geometry better describes the inflation induced by $\Delta Pe_e$ within magma chambers, with the formation of the stress arch in the $\sigma_3$ plot. It is worth noting that for both single and dual magma chamber models, changing $\Delta Pe$ from 10 to 20 MPa slightly affects the magnitude of the stress but not its general pattern (Appendices 1 and 2).

The presence of dykes in the magma feeding system dramatically changes the $\sigma_3$ and $\sigma_1$ patterns (Fig. 6), which become quite homogeneous throughout the computational domain, with the only exception of sidewall effects induced by the zero displacement conditions.

The addition of extensional field stress of 5 MPa reduces the sidewall effects and produces an almost homogeneous stress distribution in the upper part of the computational domain, above the top of the deep magma chamber. This, along with the additional inclusion of the damage zones introduced to mimic the effects of CR faults, describes a volcanic system close to equilibrium, in which pressure within the volcano feeding system almost equilibrates the lithostatic stress (Sulpizio et al., 2016).

*6.2 Some implications of the stress state of the CVC inferred from FEM*

The results from the most complete FEM runs highlight an almost homogeneous stress distribution in the CVC area. This means the dual magma chamber model and the application of far-field stress provide a stable geometry, which limits the stress changes to a few MPa. The majority of stress variations are located at the tips of the magma chambers, as expected for pressurized or under-pressurized cavities in the lithosphere (Martí and Geyer, 2009), implying that the whole feeding system is in a quasi-equilibrium state. Even if we consider the scenario of complete emptying of the upper conduit and part of the shallow magma chamber, as occurred occasionally during the past sub-Plinian and Plinian eruptions (Luhr et al., 2002; Saucedo et al., 2010; Massaro et al., 2018), this would result in the restoration of the stress arch, which is still a stable stress configuration. Even complete emptying of the shallow magma chamber would probably be ineffective for triggering a large collapse (caldera-forming) of the feeding system.

Beside and beyond the limitations due to the first-order approximation of the FEM analysis, other sources of uncertainty in the discussion about the present and future stress state of the CVC come from not considering gravity-driven processes, such as volcano spreading due to plastic deformation of Unit GF (Norini et al., 2010, 2019) and detailed regional tectonics (Norini et al., 2010, 2019). The effect of the two fault systems bordering the CR is here simulated by degrading the mechanic properties of rocks in an area of about 1 km width up to a depth of 10 km. Although the effects are negligible at the scale of the computational domain, it cannot be excluded that some local significant effects that cannot be resolved using the described approach.

## 7 Summary and conclusion

The presented study highlights the importance of using complete and detailed geological and geophysical data when dealing with FEM of volcanic areas. The different geological detail used in the model runs showed how the stress pattern depends critically on the geometry of the volcano feeding system, with huge differences in having a single or double magma chamber system and, in particular, whether or not the magma chamber(s) are connected to the surface by feeder dykes and conduits. The geometry of the feeding system is prevalent on model outputs with respect to varying rock properties (i.e. Young modulus) of one order of magnitude. In the case of CVC, the use of subsurface homogeneous or stratified lithology does not influence the FEM outputs much, the subsurface geology of the computational domain being dominated by carbonates (Unit B).

Beside and beyond the results obtained by analysing the influence of detailed geological and geophysical data, the presented modelling confirms the close to equilibrium state of the volcano, which is the expected stress distribution induced by a feeding system directly connected to the surface. The Complete emptying of the upper conduit and part of the shallow magma chamber, as occurred occasionally in the past, originating sub-Plinian and Plinian eruptions, would result in restoration of the stress arch, which is still a stable stress configuration. It follows that large magnitude, caldera-forming eruptions are possible only if the bigger deep magma chamber is also involved and significantly emptied during an eruption.

## Tables

**Table 1 -** Element types used in LISA analysis considering the final conduit feeding system configuration – Fig.1d, panel vi)

| *E-W cross-section (a-a')* | | Element Type | Elements | Nodes |
|---|---|---|---|---|
| FC | Fuego de Colima | quad4-tri3 | 372 | 384 |
| VD | Volcanic Deposits | quad4-tri3 | 245 | 273 |
| GF | Graben Fill | quad4-tri3 | 456 | 338 |
| B | Basament | quad4-tri3 | 3088 | 2907 |
| CG | Colima graben | quad4-tri3 | 48 | 71 |

Total Elements: 4209

**Table 2 -** Rock mass and mechanical properties of the geological Units used in the finite-element model (from Norini et al., 2010, 2019).

| **Acronym** | **Model Unit** | **Rock Type** | **Density ($kg/m^3$)** | **Young's Modulus (MPa)** | **Poisson's ratio *ν*** |
|---|---|---|---|---|---|
| FC | Fuego de Colima | Andesitic lavas and pyroclastic deposits forming the Paleofuego-Fuego de Colima volcano | 2242 | $1.4 \times 10^3$ | 0.30 |

| | | | | | |
|---|---|---|---|---|---|
| VD | Volcaniclastic deposits | Pyroclastic and epiclastic deposits covering the southern flank of the CVC | 1539 | $1.7 \times 10^3$ | 0.32 |
| GF | Graben Fill | Quaternary alluvial, colluvial, lacustrine deposits filling the graben | 1834 | $1.5 \times 10^3$ | 0.35 |
| B | Basement | Cretaceous limestones and intrusive rocks forming the bed-rock underlying the CVC | 2650 | $3.6 \times 10^4$ | 0.30 |

## Appendices

### Appendix 1

E–W gravitational modelling of the CVC domain (stratified lithology) for all configurations investigated. The magnitude and pattern of the principal stress account for a) single magma chamber model (4426 nodes: 4426); b) dual magma chamber model (number of nodes: 4161 nodes); c) dual magma chamber with conduits model (number of nodes: 3737 nodes). The Dimensions of the deep magma chamber: *2a* = 14 km and *2b* = 3.6 km at 15 km of depth; shallow magma chamber: *2a* = 3.5 km and *2b* = 2 km at 6 km. $\Delta P_e$ and $\Delta P_o$ equal to= 20 MPa for the deep chamber, and 5 MPa for the shallower. Black dotted lines highlight the passage from different stress values. Note that the scales of stress values are different for each panel in order to maximizse the simulation details.

### Appendix 2

E–W gravitational modelling of the CVC domain (stratified lithology) considering an extensional far field of 5 MPa for all configurations investigated. The magnitude and pattern of the principal stress account for a) single magma chamber model (nodes: 4426 nodes); b) dual magma chamber model (number of nodes: 4161 nodes); c) dual magma chamber with conduits model (number of elements: 3737 nodes). The Dimensions of the deep magma chamber: *2a* = 14 km and *2b* = 3.6 km at 15 km depth; shallow magma chamber: *2a* = 3.5 km and *2b* = = 2 km at 6 km. $\Delta P_e$ and $\Delta P_o$ are equal to= 20 MPa for the deep chamber, and 5 MPa for the shallower. Black dotted lines highlight the passage from different stress values. The Red arrows indicate the direction of the applied far-field stress. Note that the scales of stress values are different for each panel in order to maximizse the simulation details.

## Figure Captions

**Fig. 1** (a) Morphotectonic map of the Colima Volcanic Complex (NC = Nevado de Colima volcano; FC = Fuego de Colima volcano) and Colima Rift with the main tectonic and volcano-tectonic structures (NCG = Northern Colima Graben; CCG = Central Colima Graben, from Norini et al., 2019). Inset: the location of the Colima Volcanic Complex (CVC) within the Trans-Mexican Volcanic Belt (TMVB) is shown in the frame of the subduction-type geodynamic setting of Central America (from Davìla et al., 2019); (b) general sketch of the geometrical configurations used in LISA; (c) example of mesh of the investigated area for the dual magma chamber model with conduits (case v in panel (b), considering zero displacement along the bottom and left and right sides. Note that for case (vi) in panel (b) the zero displacement is removed from the lateral sides; (d) sketch of the Fuego de Colima feeding system composed of a 15 km-deep magma chamber connected to the surface via a 6 km-deep magma chamber and dykes. $\Delta P_{chs}$ and $\Delta P_{chd}$ indicate either excess or over pressure (depending on the model used) in the shallow and deep chambers, respectively (modified from Massaro et al., 2019).

**Fig. 2** Results of the sensitivity analysis carried out on the Young modulus variations within each rock layer of the domain considering different configurations (stratified substratum model – 4426 nodes4426; single magma chamber model – 4426 nodes: 4426; dual magma chamber model – 4161 nodes: 4161; dual magma chamber with conduits model – 3737 nodes: 3737). For each geological unit (B, FC, GF, VD), the relative global variation in $L_2$ (%) is provided for $\sigma_1$ and $\sigma_3$. The *x*(−-) and *x*(+) vectors indicate the variation in Young's modulus variation by an order of magnitude with respect to the *xref* vector, containing the stress values calculated by using the values of the material's properties indicated in Table 2.

**Fig. 3** Spatial variation (%) of the $L_2$ norm's components at varying Young modulus for selected cases of Units B and VD: (a) Unit B in the stratified substratum model (4426 nodes); (b) Unit B in the single magma chamber model (4426 nodes); (c) Unit B in the dual magma chamber model (4161 nodes); (d) Unit VD in the dual magma chamber with conduits model (nodes: 3737 nodes). Symbols *x(-)* (−) and *x*(+) have the same meaning as inof Figure 2.

**Fig. 4** E–W gravitational modelling of the CVC domain. The scale of the mesh is expressed in units of design (1 UD = 1 km). The domain extends 60 km along the *x*-axis, and 30 km along the *z*-axis. The number of nodes used in the mesh is set to 4426. The magnitude and pattern of the principal stresses (dotted black lines) are reported for (a) homogeneous stratigraphy (Unit FC = andesitic lavas and pyroclastic deposits) and (b) non-homogeneous stratigraphy (Unit FC; Unit B = Cretaceous limestone and intrusive rocks forming the bedrock underlying the CVC; Unit GF = Quaternary alluvial, colluvial and lacustrine deposits filling the graben; Unit VD = volcaniclastic deposits covering the southern flank of the CVC). The blue line contours the unperturbed part of the domain, which extends ca. 30 km horizontally and ca. 25 km vertically. Note that the scale of stress values is the same for all simulations.

**Fig. 5** E–W gravitational modelling of the CVC domain with non-homogeneous stratigraphy. The magnitude and pattern of the principal stresses are reported for (a) the single magma chamber model represented by a magma chamber ($2a$ = 14 km and $2b$ = 3.6 km) at 15 km depth, and (b) the dual magma chamber model composed of a 15 km-deep magma chamber ($2a$ = 14 km and $2b$ = 3.6 km) and a shallow 6 km-deep one ($2a$ = 3.5 km and $2b$ = 2 km). The magma chambers are not connected. $\Delta Po$ is set to 10 and 5 MPa for the 15 km-deep and 6 km-deep magma chambers, respectively. The number of nodes is set to 4426 and 4161 for the single and dual magma chamber models, respectively. Black dotted lines highlight the passage from different stress values. The red dotted line in panel (bi) indicates the formation of the stress arch. Note that the scale of stress values is different for each panel in order to maximizse the simulation details.

**Fig. 6** E–W gravitational modelling of the CVC domain with non-homogeneous stratigraphy accounting for a dual magma chamber system connected by dykes via the surface (deep magma chamber, $2a$ = 14 km and $2b$ = 3.6 km at 15 km depth; shallow magma chamber, $2a$ = 3.5 km and $2b$ = = 2 km at 6 km od depth). The magnitude and pattern of the principal stresses are shown. The number of nodes used is set to 3737. $\Delta Po$ is set to 10 and 5 MPa for the 15 km-deep and 6 km-deep magma chambers, respectively. The black dotted lines in panel (ii) highlight the passage from different stress values. Note that the scale of stress values are is different for each panel in order to maximizse the simulation details.

**Fig. 7** E–W gravitational modelling of the CVC domain with non-homogeneous stratigraphy considering the extensional field stress. The magnitude and pattern of the principal stresses are shown for the single magma chamber model (panels i and -ii), the dual magma chamber model (panels iii and-iv) and, the dual magma chamber with conduits model (panels v-vi-vii-–viii). Note that in panels vii and -viii the faults bordering the CG are shown. For all configurations, an extensive far-field stress of 5 MPa is applied at the lateral boundaries of the domain. In panels vii and- viii, the additional effect of the local extensive field is simulated using a reduced values of material properties (Table 2). $\Delta Po$ is set to 10 and 5 MPa for the 15 km-deep and 6 km-deep magma chambers, respectively. Black dotted lines highlight the passage from different stress values. The red arrows indicate the direction of the applied far- field stress. Note that the scale of stress values is different for each panel in order to maximizse the simulation details.

Figure 1

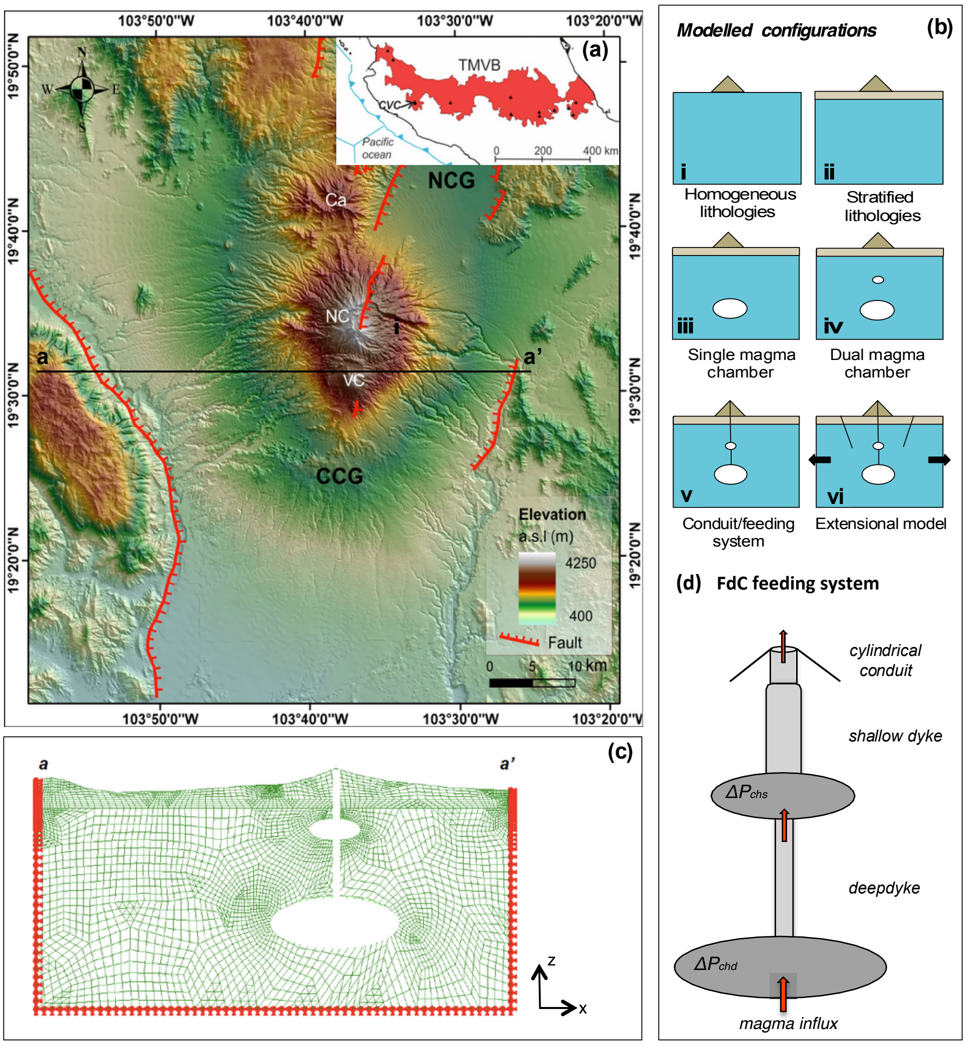
103°50'0"W
103°40'0"W
103°30'0"W
103°20'0"W
19°50'0"N
19°40'0"N
19°30'0"N
19°20'0"N
(a)
N
S
E
W
TMVB
CVC
Pacific ocean
0
200
400 km
NCG
Ca
NC
VC
a
a'
CCG
Elevation
a.s.l (m)
4250
400
Fault
0
5
10 km
Modelled configurations
(b)
i
Homogeneous lithologies
ii
Stratified lithologies
iii
Single magma chamber
iv
Dual magma chamber
v
Conduit/feeding system
vi
Extensional model
(c)
a
a'
z
x
(d) FdC feeding system
cylindrical conduit
shallow dyke
ΔPchs
deepdyke
ΔPchd
magma influx

Figure 2

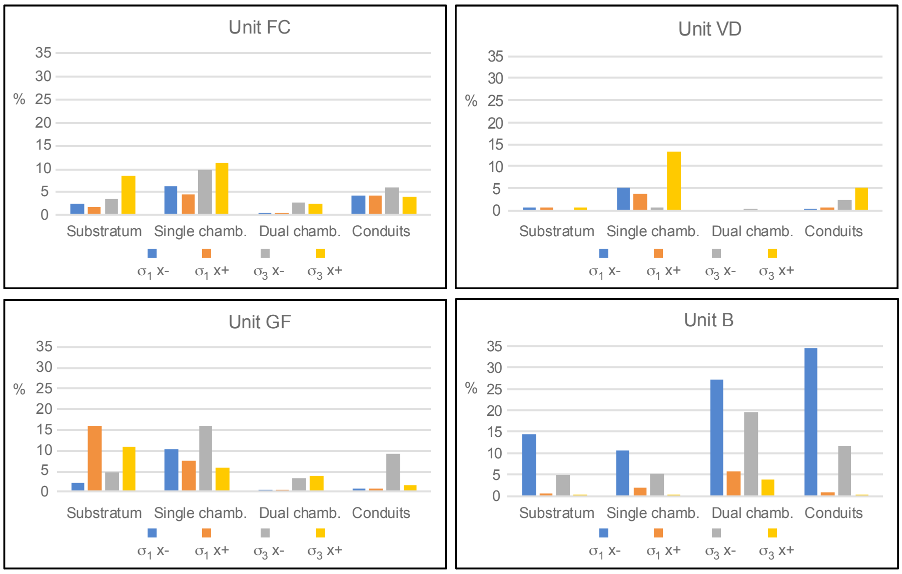
Unit FC
Unit VD
Unit GF
Unit B
%
35
30
25
20
15
10
5
0
Substratum
Single chamb.
Dual chamb.
Conduits
σ1 x-
σ1 x+
σ3 x-
σ3 x+

Figure 3

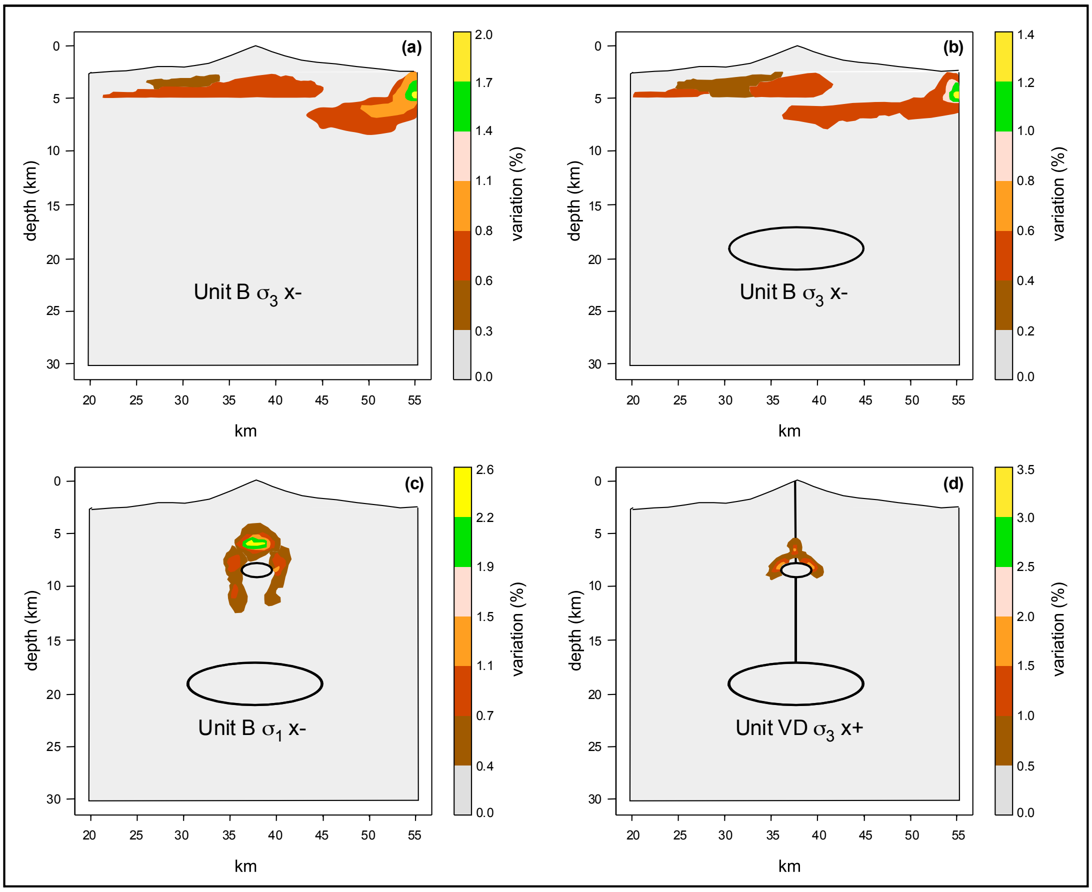

(a)
Unit B σ3 x-
(b)
Unit B σ3 x-
(c)
Unit B σ1 x-
(d)
Unit VD σ3 x+
depth (km)
km
variation (%)


Figure 4

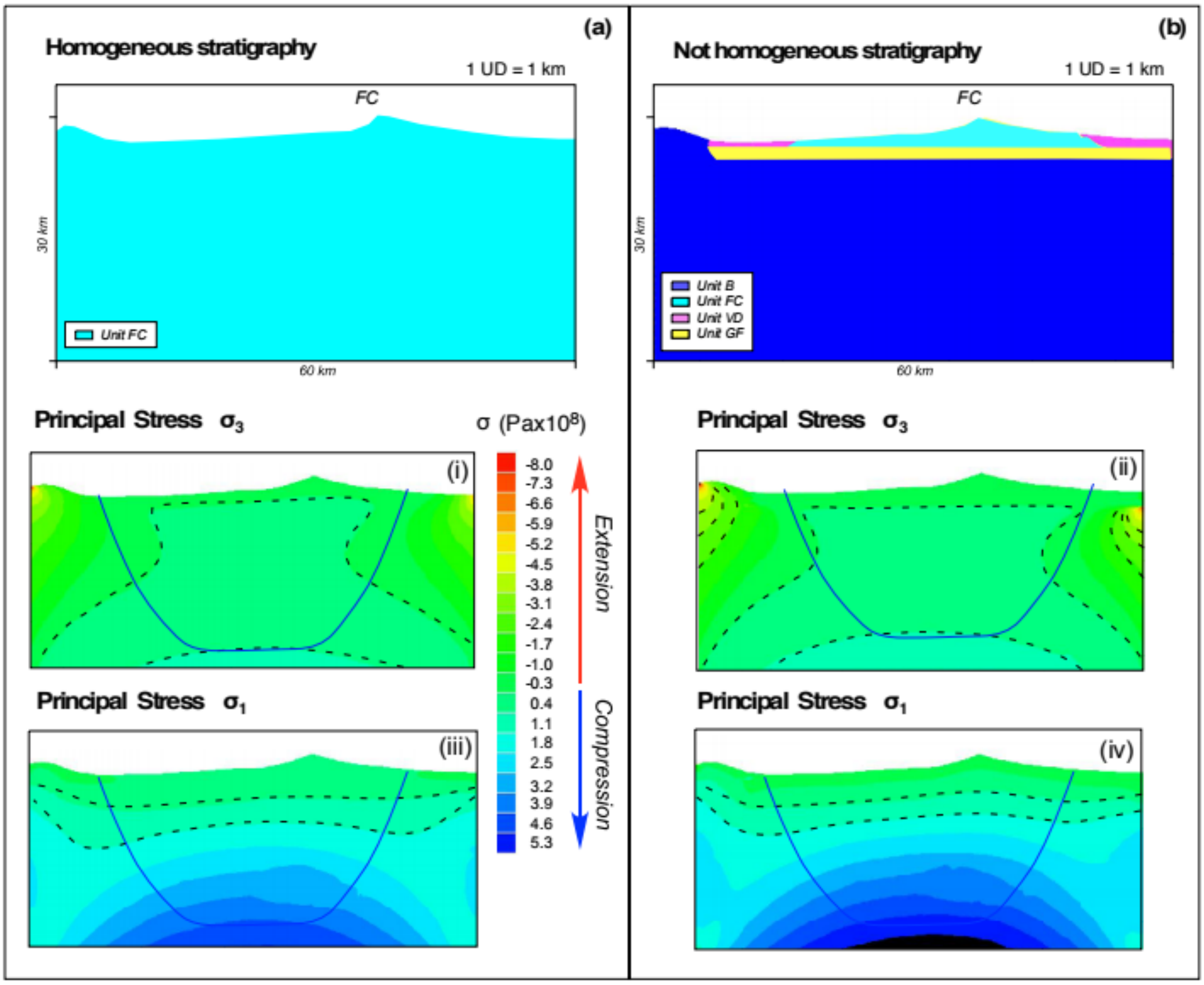

Homogeneous stratigraphy
(a)
1 UD = 1 km
FC
30 km
Unit FC
60 km
Not homogeneous stratigraphy
(b)
1 UD = 1 km
FC
30 km
Unit B
Unit FC
Unit VD
Unit GF
60 km
Principal Stress σ3
σ (Pax10^8)
(i)
(ii)
-8.0
-7.3
-6.6
-5.9
-5.2
-4.5
-3.8
-3.1
-2.4
-1.7
-1.0
-0.3
0.4
1.1
1.8
2.5
3.2
3.9
4.6
5.3
Extension
Compression
Principal Stress σ1
(iii)
(iv)


Figure 5

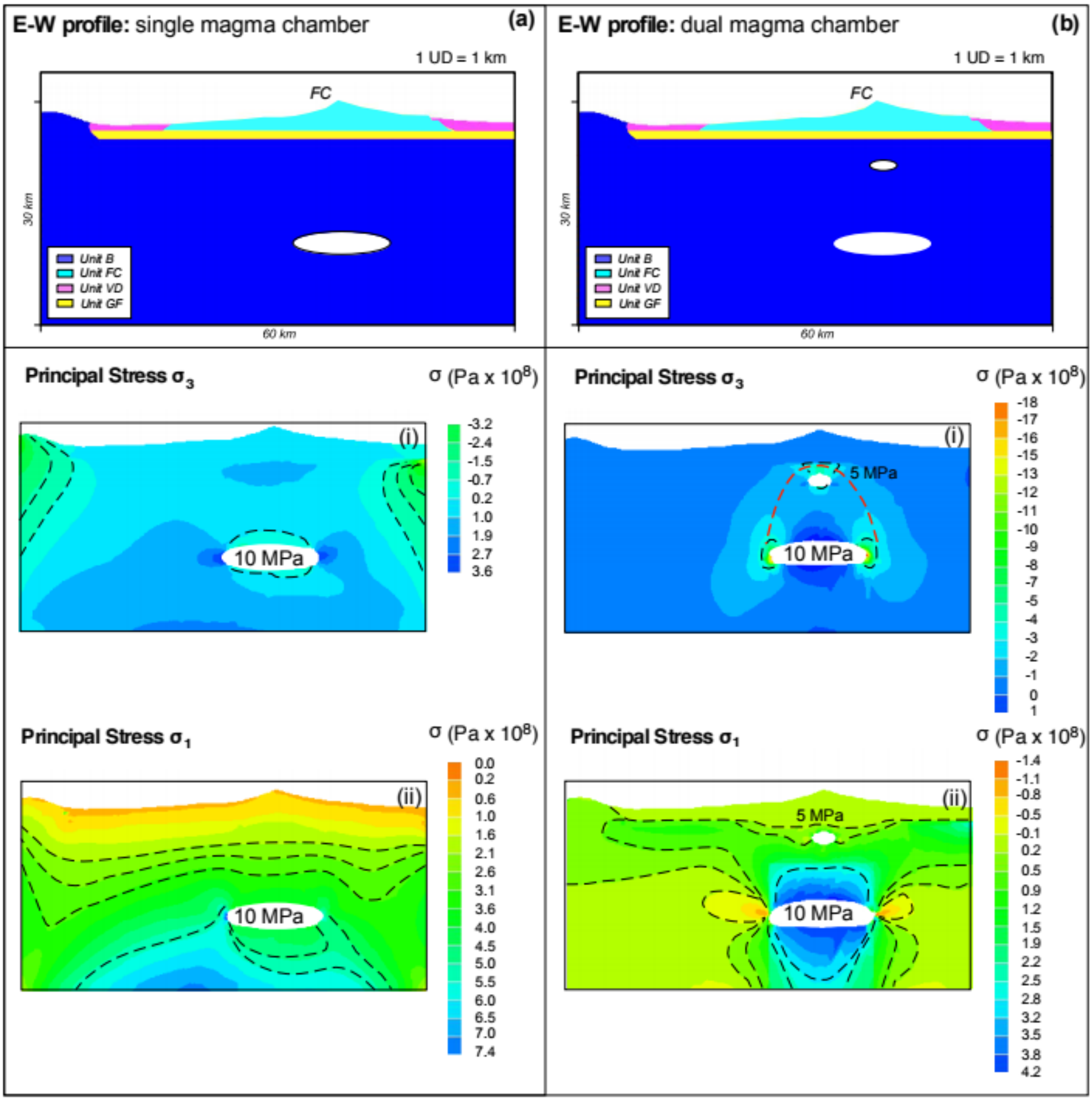
E-W profile: single magma chamber
(a)
1 UD = 1 km
FC
30 km
60 km
Unit B
Unit FC
Unit VD
Unit GF
E-W profile: dual magma chamber
(b)
1 UD = 1 km
FC
30 km
60 km
Unit B
Unit FC
Unit VD
Unit GF
Principal Stress σ3
σ (Pa x 10^8)
(i)
10 MPa
-3.2
-2.4
-1.5
-0.7
0.2
1.0
1.9
2.7
3.6
Principal Stress σ3
σ (Pa x 10^8)
(i)
5 MPa
10 MPa
-18
-17
-16
-15
-13
-12
-11
-10
-9
-8
-7
-5
-4
-3
-2
-1
0
1
Principal Stress σ1
σ (Pa x 10^8)
(ii)
10 MPa
0.0
0.2
0.6
1.0
1.6
2.1
2.6
3.1
3.6
4.0
4.5
5.0
5.5
6.0
6.5
7.0
7.4
Principal Stress σ1
σ (Pa x 10^8)
(ii)
5 MPa
10 MPa
-1.4
-1.1
-0.8
-0.5
-0.1
0.2
0.5
0.9
1.2
1.5
1.9
2.2
2.5
2.8
3.2
3.5
3.8
4.2

Figure 6

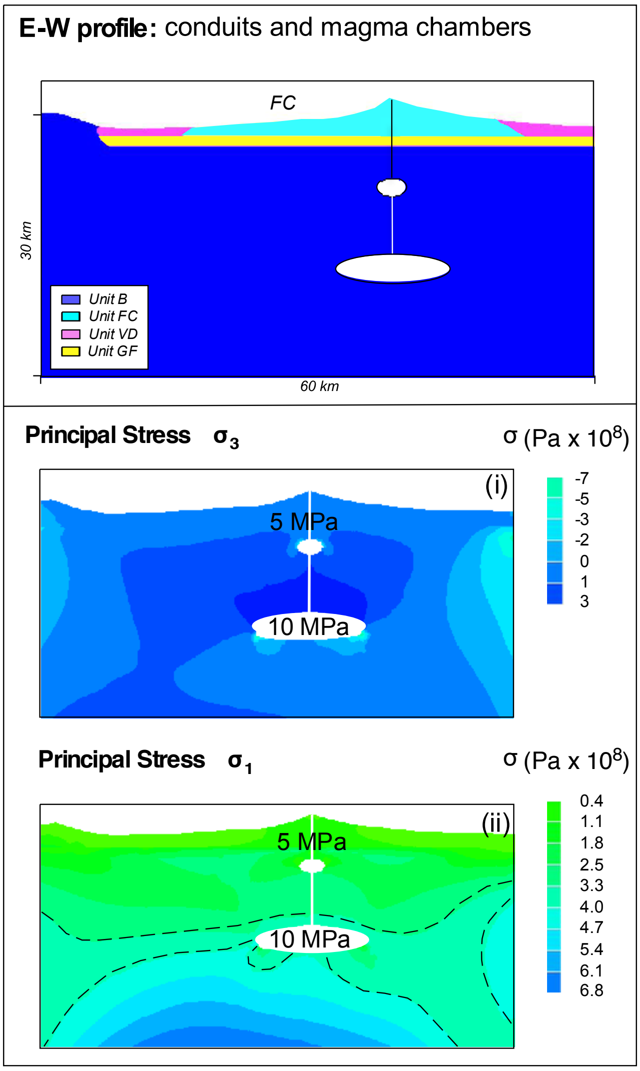
E-W profile: conduits and magma chambers
FC
30 km
60 km
Unit B
Unit FC
Unit VD
Unit GF
Principal Stress σ3
σ (Pa x 10^8)
(i)
5 MPa
10 MPa
-7
-5
-3
-2
0
1
3
Principal Stress σ1
σ (Pa x 10^8)
(ii)
5 MPa
10 MPa
0.4
1.1
1.8
2.5
3.3
4.0
4.7
5.4
6.1
6.8

Figure 7

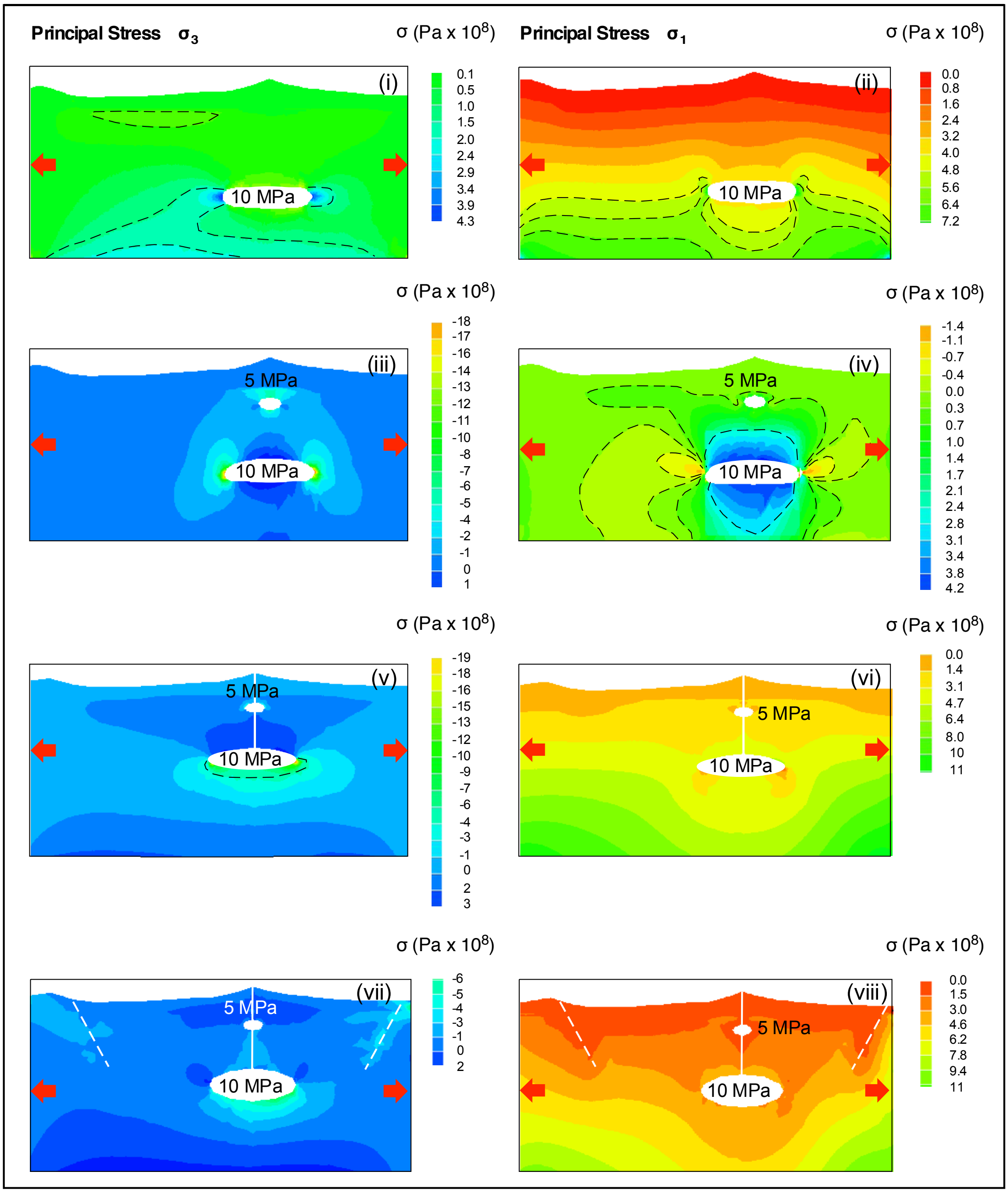
Principal Stress σ3
Principal Stress σ1
σ (Pa x 10^8)
(i)
(ii)
(iii)
(iv)
(v)
(vi)
(vii)
(viii)
10 MPa
5 MPa

Appendix 1

## Appendix 1

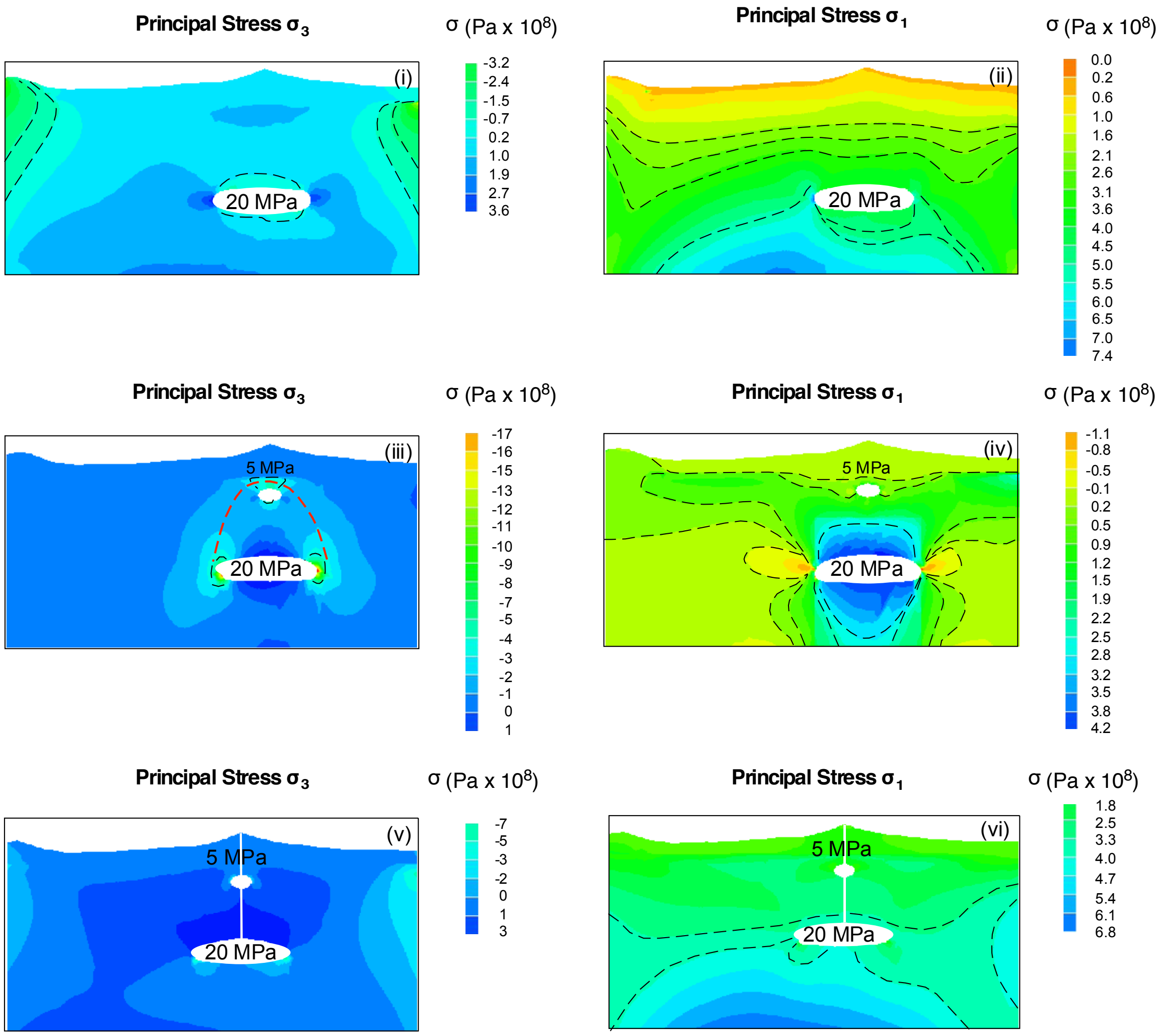


Appendix 2

## Appendix 2

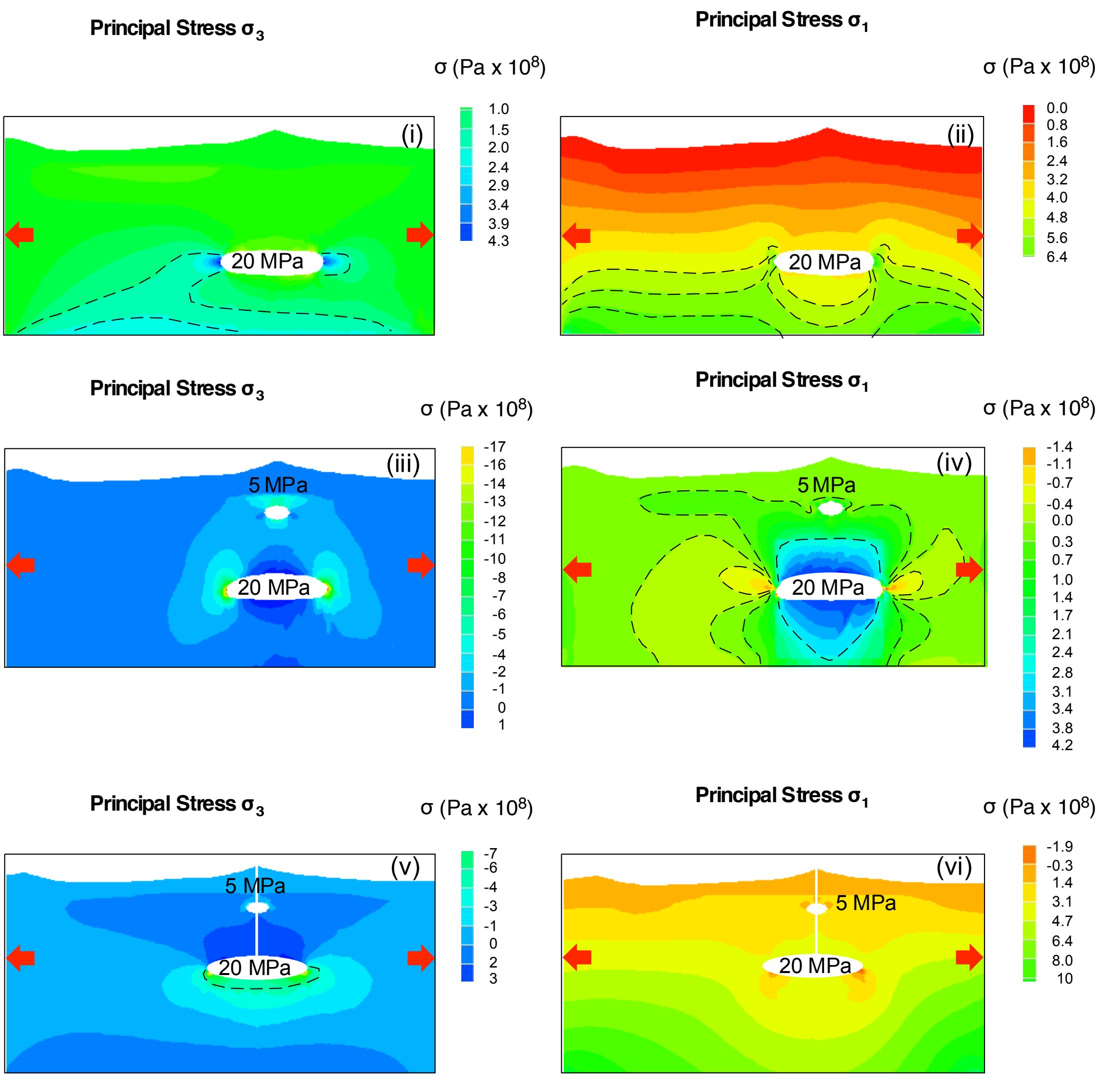


### Code/Data Avaiability

The LISA code is available at https://lisafea.com/.

### Author's contribution

SM, RS, AC, GN and GG conceived the study. SM and RS wrote the bulk of the manuscript with the input of all the co-authors. SM and GL compiled the numerical simulations and formulated the adopted methodology. MP and SM carried out the sensitivity analysis. All authors worked on the interpretation of the results.

**Competing interests:** The authors declare that they have no conflict of interest.

**Acknowledgements:** The manuscript received a professional copy-editing. SM thanks the LISA customer service for the support received. In particular, Karl.

## References

Albino, F., Pinel, V., and Sigmundsson, F., 2010. Influence of surface load variations on eruption likelihood: application to two Icelandic subglacial volcanoes, Grímsvötn and Katla. Geophysical journal international, 181(3), 1510-1524.

Albino, F., Amelung, F., and Gregg, P., 2018. The role of pore fluid pressure on the failure of magma reservoirs: insights from Indonesian and Aleutian arc volcanoes. Journal of Geophysical Research: Solid Earth, 123(2), 1328-1349.

Anderson E.M., 1936. The dynamics of formation of cone sheets, ring dykes and cauldron subsidence. Proc R Soc Edinburgh 56:128–163.

Allan, J.F., 1985. Sediment depth in the NCG from 3-D interpretation of gravity. Geofis. Int. 24, 21–30 (1985).

Allan, J.F. 1986. Geology of the Northern Colima and Zacoalco grabens, Southwest Mexico: Late Cenozoic rifting in the Mexican Volcanic Belt. Geol. Soc. Am. Bull. 97, 473–485

Allan, J.F., Nelson, S.A., Luhr, J.F., Charmichael, I.S.E., Wopat, M., Wallace, P.J., 1991: Pliocene-Holocene rifting and associated volcanism in Southwest Mexico: an exotic terrane in the making. In: Dauphin, J.P., Simoneit, R.R.T. (eds.) The Gulf and Peninsular Provinces of the Californias, AAPG Mem., vol. 47, pp. 425–445.

Andrew, R.E., and Gudmundsson, A., 2008. Volcanoes as elastic inclusions: Their effects on the propagation of dykes, volcanic fissures, and volcanic zones in Iceland. Journal of Volcanology and Geothermal Research, 177(4), 1045-1054.

Arámbula-Mendoza, R., Reyes-Dávila, G., Dulce, M.V.B., González-Amezcua, M., Navarro- Ochoa, C., Martínez-Fierros, A., and Ramírez-Vázquez, A., 2018. Seismic monitoring of effusive-explosive activity and large lava dome collapses during 2013–2015 at Volcán de Colima, Mexico. J. Volcanol. Geotherm. Res., 351, 75-88.

Babuška, I., Ihlenburg, F., Paik, E. T., and Sauter, S.A., 1995. A generalized finite element method for solving the Helmholtz equation in two dimensions with minimal pollution. Computer methods in applied mechanics and engineering, 128(3-4), 325-359.

Bandy, W.L., Mortera-Gutiérrez, C.A., Urrutia- Fucugauchi, J., Hilde, T.W.C, 1995. The subducted Rivera-Cocos plate boundary: where is it, what is it, and what is its relationship to the Colima Rift?

Geophys. Res. Lett. 22, 3075–3078.

Barrier, B., Bourgois, J., Michaud, F., 1990: The active Jalisco triple junction rift system. C.R. Acad. Sci. Paris, 310 (II), 1513–1520.

Bathe, K. J., Zhang, H., and Ji, S., 1999. Finite element analysis of fluid flows fully coupled with structural interactions. Computers and Structures, 72(1-3), 1-16.

Bonafede, M., Parenti, B., Rivalta, E., 2002. On strike-slip faulting in layered media. Geophysical Journal International, 149(3), 698-723.

Bonasia R, Capra L, Costa A, Macedonio G, Saucedo R., 2011. Tephra fallout hazard assessment for a Plinian eruption scenario at Volcan de Colima. J Volcanol Geotherm Res 203: 12–22.

Boresi, A.P., Schmidt, R.J., and Sidebottom, O.M., 1985. Advanced mechanics of materials (Vol. 6). New York et al.: Wiley.

Buchmann T. and Conolly P.T., 2007. Contemporary kinematics of the Upper Rhine Graben: A 3D finite element approach. Global and Planetary Change 58, 287–309.

Bunney, 2014. The Effects of Structural Heterogeneities and In-elastic Rheology on Ground Deformation at Campi Flegrei Caldera, Italy. PhD Thesis.

Cabaniss, H.E., Gregg, P. M., and Grosfils, E.B., 2018. The role of tectonic stress in triggering large silicic caldera eruptions. Geophysical Research Letters, 45, 3889–3895. https://doi.org/10.1029/ 2018GL077393 .

Cayol, V., and Cornet, F. H., 1998. Effects of topography on the interpretation of the deformation field of prominent volcanoes: Applicationto Etna.Geophysical Research Letters,25(11), 1979–1982. https://doi.org/10.1029/98GL51512.

Cailleau, B., T.R. Walter, P. Janle, and E. Hauber, 2003. Modeling volcanic deformation in a regional stress field: Implications for the formation of graben structures on Alba Patera, Mars, J. Geophys. Res., 108(E12), 5141, doi:10.1029/2003JE002135.

Cailleau B., Thomas R. Walter, Peter Janle, Ernst Hauber, 2005. Unveiling the origin of radial grabens on Alba Patera volcano by finite element modelling Icarus 176, 44–56.

Cabrera-Gutiérrez, R., and Espíndola, J.M., 2010. The 1998-1999 eruption of Volcán de Colima, Mexico: an application of Maeda's viscoelastic model. Geofísica internacional, 49(2), 83-96.

Canales, J.P., Nedimović, M.R., Kent, G.M., Carbotte, S.M., and Detrick, R.S., 2009. Seismic reflection images of a near-axis melt sill within the lower crust at the Juan de Fuca ridge. Nature, 460(7251), 89.

Capra, L., and Macıas, J.L., 2002. The cohesive Naranjo debris-flow deposit (10 $km^3$): A dam breakout flow derived from the Pleistocene debris-avalanche deposit of Nevado de Colima Volcano (México). Journal of Volcanology and Geothermal Research, 117(1-2), 213-235.

Capra L, Macías JL, Cortés A, Dávila N, Saucedo R, Osorio-Ocampo S, Arce JL, Galvilanes-Ruiz JC, Corona-Càvez P, Gàrcia-Sancez L, Sosa-Ceballos G, Vasquez R., 2016. Preliminary report on the July 10–11, 2015 eruption at Volcán de Colima: Pyroclastic density currents with exceptional runouts and volume, J Volcanol Geotherm Res 310: 39-49.

Cianetti, S., Giunchi, C., and Casarotti, E., 2012. Volcanic deformation and flank instability due to magmatic sources and frictional rheology: the case of Mount Etna. Geophysical Journal International, 191(3), 939-953.

Charco, M., and Galán del Sastre, P., 2014. Efficient inversion of three-dimensional finite element models of volcano deformation. Geophysical Journal International, 196(3), 1441-1454.

Chaput, M., Pinel, V., Famin, V., Michon, L., and Froger, J.L., 2014. Cointrusive shear displacement by sill intrusion in a detachment: A numerical approach. Geophysical Research Letters, 41(6), 1937-1943.

Cortés, A., 2005. Carta geológica del complejo volcánico de Colima. UNAM, Instituto de Geología.

Cortés, A., Garduño, V.H., Macías, J. L., Navarro-Ochoa, C., Komorowski, J.C., Saucedo, R., and Gavilanes, J. C. (2010). Geologic mapping of the Colima volcanic complex (Mexico) and implications for hazard assessment. Geol Soc Am Spec Pap, 464, 249-264.

Cortés, A., Komorowski, J. C., Macías, J. L., Capra, L., and Layer, P. W., 2019. Late Pleistocene-Holocene debris avalanche deposits from Volcán de Colima, Mexico. In Volcán de Colima (pp. 55-79). Springer, Berlin, Heidelberg.

Costa, A., Sparks, R.S.J., Macedonio, G., and Melnik, O., 2009. Effects of wall-rock elasticity on magma flow in dykes during explosive eruptions. Earth and Planetary Science Letters, 288(3-4), 455-462.

Costa, A., Gottsmann, J., Melnik, O., and Sparks, R. S. J., 2011. A stress-controlled mechanism for the intensity of very large magnitude explosive eruptions. Earth and Planetary Science Letters, 310(1-2), 161-166.

Currenti, G., Bonaccorso, A., Del Negro, C., Scandura, D., and Boschi, E., 2010. Elasto-plastic modeling of volcano ground deformation. Earth and Planetary Science Letters, 296(3-4), 311-318.

Currenti, G., and Williams, C.A., 2014. Numerical modeling of deformation and stress fields around a magma chamber: Constraints on failure conditions and rheology. Physics of the Earth and Planetary Interiors, 226, 14-27.

Dávila, N., Capra, L., Ferrés, D., Gavilanes-Ruiz, J. C., and Flores, P., 2019. Chronology of the 2014–2016 Eruptive Phase of Volcán de Colima and Volume Estimation of Associated Lava Flows and Pyroclastic Flows Based on Optical Multi-Sensors. Remote Sensing, 11(10), 1167.

Del Potro, R. and Hürlimann, M., 2008. Geotechnical classification and characterization of materials for stability analyses of large volcanic slopes. Eng. Geol. 98(1), 1–17.

Dieterich J.H., and R.W. Decker, 1975. Finite element modeling of surface deformation associated with volcanism, J. Geophys. Res., 80, 4094–4102.

Escudero, C.R., and Bandy, W.L., 2017: Ambient seismic noise tomography of the Colima Volcano Complex. Bull. Volcanol. 79, 13.

Fernández, J., Tiampo, K. F., Jentzsch, G., Charco, M., and Rundle, J.B., 2001. Inflation or deflation? New results for Mayon Volcano applying elastic-gravitational modeling. Geophysical Research Letters, 28(12), 2349-2352.

Ferrari, L., Rosas-Elguera, J., Márquez, A., Oyarzun, R., Doblas, M., and Verma, S.P., 1999. Alkalic (ocean-island basalt type) and calc-alkalic volcanism in the Mexican volcanic belt: A case for plume-related magmatism and propagating rifting at an active margin?: Comment and Reply. Geology, 27(11), 1055-1056.

Folch, A., Fernández, J., Rundle, J.B., Martí, J., 2000. Ground deformation in a viscoelastic medium composed of a layer overlying a half-space: a comparison between point and extended sources. Geophys. J. Int. 140 (1), 37–50.

Frey, H.M., Lange, R.A., Hall, C.M., Delgado-Granados, H., Carmichael, I.S.E., 2007. A Pliocene ignimbrite flare-up along the Tepic-Zacoalco rift: evidence for the initial stages of rifting between the Jalisco block (Mexico) and North America. Geol. Soc. Am. Bull. 119, 49–64. http://dx.doi.org/10.1130/B25950.1.

Fujita, E., Kozono, T., Ueda, H., Kohno, Y., Yoshioka, S., Toda, N., and Ida, Y., 2013. Stress field change around the Mount Fuji volcano magma system caused by the Tohoku megathrust earthquake, Japan. Bulletin of volcanology, 75(1), 679.

Gabrieli, A., Wilson, L., and Lane, S., 2015. Volcano–tectonic interactions as triggers of volcanic eruptions. Proceedings of the Geologists' Association, 126(6), 675-682.

Garduño-Monroy, V.H., Saucedo-Girón, R., Jiménez, Z., Gavilanes-Ruiz, J.C., Cortés-Cortés, A., Uribe-Cifuentes, R.M. 1998: La Falla Tamazula, límite suroriental del Bloque Jalisco, y sus relaciones con el Complejo Volcánico de Colima, México. Revista Mexicana de Ciencias Geológicas 15(2), 132–144.

Gelman, S.E., Deering, C.D., Gutierrez, F.J., and Bachmann, O., 2013. Evolution of the Taupo Volcanic Center, New Zealand: petrological and thermal constraints from the Omega dacite. Contributions to Mineralogy and Petrology, 166(5), 1355-1374.

Geyer, A., and Martí, J., 2009. Stress fields controlling the formation of nested and overlapping calderas: implications for the understanding of caldera unrest. Journal of Volcanology and Geothermal Research, 181(3-4), 185-195.

Geyer, A., and Gottsmann, J., 2010. The influence of mechanical stiffness on caldera deformation and implications for the 1971–1984 Rabaul uplift (Papua New Guinea). Tectonophysics, 483(3-4), 399-412.

Geyer, A., Martí, J., and Villaseñor, A., 2016. First-order estimate of the Canary Islands plate-scale stress field: Implications for volcanic hazard assessment. Tectonophysics, 679, 125-139.

Gerbault, M., Cappa, F., Hassani, R., 2012. Elasto-plastic and hydromechanical models of failure around an infinitely long magma chamber. Geochem. Geophys. Geosyst. 13, Q03009. http://dx.doi.org/10.1029/2011GC003917.

Gerbault, M., Hassani, R, Lizama CN, Souche, A., 2018. Three-Dimensional Failure Patterns Around an Inflating Magmatic Chamber. Geochemistry, Geophysics, Geosystems, AGU and the Geochemical Society, In press.

Geshi, N., Kusumoto, S., and Gudmundsson, A., 2012. Effects of mechanical layering of host rocks on dike growth and arrest. Journal of Volcanology and Geothermal Research, 223, 74-82.

Grosfils, E.B., 2007. Magma reservoir failure on the terres- trial planets: Assessing the importance of gravitational loading in simple elastic models, J. Volcanol. Geotherm. Res., 166, 47–75, doi:10.1016/j.jvolgeores.2007.06.007.

Grosfils, E.B., McGovern, P. J., Gregg, P.M., Galgana, G.A., Hurwitz, D.M., Long, S.M., Chestler, S.R., 2015. Elastic models of magma reservoir mechanics: a key tool for investigating planetary volcanism. Geol. Soc. London, Spec. Pub., 401(1), 239-267.

Gudmundsson, A., and Brenner, S.L., 2004. How mechanical layering affects local stresses, unrests, and eruptions of volcanoes. Geophysical Research Letters, 31(16).

Gudmundsson, A., 2006. How local stresses control magma-chamber ruptures, dyke injections, and eruptions in composite volcanoes, Earth-Sci.Rev., 79(1–2), 1–31.

Gudmundsson, A., 2011. Rock fractures in geological processes. Cambridge University Press.

Gudmundsson, A., 2012. Strengths and strain energies of volcanic edifices: implications for eruptions, collapse calderas, and landslides. *Natural Hazards and Earth System Sciences*, *12*(7), 2241.

Goennermann and Taisne, 2015. Magma Transport in Dikes. The Encyclopedia of Volcanoes. http://dx.doi.org/10.1016/B978-0-12-385938-9.00010-9.

Gottsmann, J., Folch, A., and Rymer, H., 2006. Unrest at Campi Flegrei: A contribution to the magmatic versus hydrothermal debate from inverse and finite element modeling. Journal of Geophysical Research: Solid Earth, 111(B7).

Gutiérrez, F., and Parada, M.A., 2010. Numerical modeling of time-dependent fluid dynamics and differentiation of a shallow basaltic magma chamber. Journal of Petrology, 51(3), 731-762.

Hautmann, S., Gottsmann, J., Sparks, R.S.J., Costa, A., Melnik, O., and Voight, B., 2009. Modelling ground deformation caused by oscillating overpressure in a dyke conduit at Soufrière Hills Volcano, Montserrat. Tectonophysics, 471(1-2), 87-95.

Heap, M. J., Villeneuve, M., Albino, F., Farquharson, J. I., Brothelande, E., Amelung, F., and Baud, P., 2020. Towards more realistic values of elastic moduli for volcano modelling. Journal of Volcanology and Geothermal Research, 390, 106684.

Hickey, J., Gottsmann, J., and Mothes, P., 2015. Estimating volcanic deformation source parameters with a finite element inversion: The 2001–2002 unrest at Cotopaxi volcano, Ecuador, J. Geophys. Res. Solid Earth, 120, 1473–1486, doi:10.1002/2014JB011731.

Hoek, E. and Brown, E.T, 1997. Practical estimates or rock mass strength. Int. J. Rock Mech. Min. Sci. 34, 1165–1186.

Holohan, E.P., Schöpfer, M. P. J., and Walsh, J.J., 2015. Stress evolution during caldera collapse. Earth and Planetary Science Letters, 421, 139-151.

Huang, X., and Zhang, Z., 2012. Stress arch bunch and its formation mechanism in blocky stratified rock masses. Journal of Rock Mechanics and Geotechnical Engineering, 4(1), 19-27.

Karlstrom, L., Dufek, J., Manga, M., 2010. Magma chamber stability in arc and continental crust. J. Volcanol. Geotherm. Res. 190, 249–270.

Kinvig, H. S., Geyer, A., and Gottsmann, J., 2009. On the effect of crustal layering on ring-fault initiation and the formation of collapse calderas. Journal of Volcanology and Geothermal Research, 186(3-4), 293-304.

Jaeger, J.C., Cook, N.G., and Zimmerman, R., 2009. Fundamentals of rock mechanics. John Wiley and Sons.

Jeanne, P., Guglielmi, Y., Rutqvist, J., Nussbaum, C., and Birkholzer, J., 2017. Field characterization of elastic properties across a fault zone reactivated by fluid injection. Journal of Geophysical Research: Solid Earth, 122(8), 6583-6598.

Jellinek, A.M. and DePaolo, D.J., 2003. A model for the origin of large silicic magma chambers: precursors of caldera-forming eruptions. Bull. Volcanol. 65, 363–381.

Lister, J.R. and Kerr, R.C., 1991. Fluid-mechanical models of crack propagation and their application to magma transport in dykes. Journal of Geophysical Research 96,10,049–10,077.

Long, S.M., and Grosfils, E.B., 2009. Modeling the effect of layered volcanic material on magma reservoir failure and associated deformation, with application to Long Valley caldera, California. Journal of Volcanology and Geothermal Research, 186(3-4), 349-360.

López-Loera, H., Urrutia-Fucugauchi, J., Alva-Valdivia, L., 2011. Estudio aeromagnético del complejo volcánico de Colima, occidente de México – implicaciones tectónicas y estructurales. Revista Mexicana de Ciencias Geológicas 28, 349–370.

Lungarini, L., Troise, C., Meo, M., and De Natale, G., 2005. Finite element modelling of topographic effects on elastic ground deformation at Mt. Etna. Journal of volcanology and geothermal research, 144(1-4), 257-271.

Luhr, J.F., and Carmichael, I.S., 1985. Contemporaneous eruptions of calc-alkaline and alkaline magmas along the volcanic front of the Mexican Volcanic Belt. Geofísica Internacional, 24(1).

Luhr, J.F., and Prestegaard, K.L., 1988. Caldera formation at Volcán Colima, Mexico, by a large holocene volcanic debris avalanche. Journal of Volcanology and Geothermal Research, 35(4), 335-348.

Luhr JF., 2002. Petrology and geochemistry of the 1991 and 1998-1999 lava flows from Volcan Colima, Mexico. J Volcanol Geotherm Res 117: 169–194.

Maccaferri, F., Bonafede, M., and Rivalta, E., 2010. A numerical model of dyke propagation in layered elastic media. Geophysical Journal International, 180(3), 1107-1123.

Maccaferri, F., Bonafede, M., and  Rivalta, E., 2011. A quantitative study of the mechanisms governing dike propagation, dike arrest and sill formation. Journal of Volcanology and Geothermal Research, 208(1-2), 39-50.

Maccaferri, F., Rivalta, E., Keir, D., and Acocella, V., 2014. Off-rift volcanism in rift zones determined by crustal unloading. Nature Geoscience, 7(4), 297-300.

Maccaferri, F., Smittarello, D., Pinel, V., and Cayol, V., 2019. On the propagation path of magma-filled dikes and hydrofractures: The competition between external stress, internal pressure, and crack length. Geochemistry, Geophysics, Geosystems, 20(4), 2064-2081.

Macías, J.L., Saucedo, R., Gavilanes, J.C., Varley, N., Velasco, García S., Bursik, M.I., Vargas, Gutiérrez V., Cortés, A., 2006. Flujos piroclásticos asociados a la activi- dad explosiva del Volcán de Colima y perspectivas futuras. GEOS 25(3), 340–351.

Macìas J, Arce J, Sosa G, Gardner JE, Saucedo R., 2017. Storage conditions and magma processes triggering the 1818CE Plinian eruption of Volcán de Colima. J Volcanol GeothermRes doi:10.1016/j.jvolgeores.2017.02.025.

Macdonald, K.C., 1982. Mid-ocean ridges: fine scale tectonic, volcanic and hydrothermal pro- cesses within the plate boundary zone. Annual Review of Earth and Planetary Sciences 10, 155–190.

MacLeod, C.J., Yaouancq, G., 2000. A fossil melt lens in the Oman ophiolite: implications for magma chamber processes at fast spreading ridges. Earth and Planetary Science Letters 176, 357–373.

Manconi A., Walter TR, and Amelung, F., 2007. Effects of mechanical layering on volcano deformation. Geophys. J. Int. (2007) 170, 952–958.

Manconi, A., Longpré, M.A., Walter, T.R., Troll, V.R., Hansteen, T.H., 2009. The effects of flank collapses on volcano plumbing systems. Geology 37 (12), 1099–1102.

Marinos, P. and Hoek, E., 2000. GSI: a geologically friendly tool for rock mass strength estimation. In: Proc. GeoEng2000 Conference, Melbourne, 1422–1442.

Martí, J., and Geyer, A., 2009. Central vs flank eruptions at Teide–Pico Viejo twin stratovolcanoes (Tenerife, Canary Islands). Journal of Volcanology and Geothermal Research, 181(1-2), 47-60.

Massaro S, Sulpizio R, Costa A, Capra L., Lucchi F., 2018. Understanding eruptive style variations at calc-alkaline volcanoes: the 1913 eruption of Fuego de Colima volcano (Mexico). Bulletin of Volcanology, 80:62.

Massaro, S., Costa, A., Sulpizio, R., Coppola, D., Capra, L., 2019. Cyclic activity of Fuego de Colima volcano (Mexico): insights from satellite thermal data and non-linear models. Solid Earth, 1429-1450.

Margottini, C., Canuti, P., Sassa, K., 2013. Landslide science and practice (Vol. 1). Berlin: Springer.

Masterlark, T., Feigl, K.L., Haney, M., Stone, J., Thurber, C., and Ronchin, E., 2012. Nonlinear estimation of geometric parameters in FEMs of volcano deformation: Integrating tomography models and geodetic data for Okmok volcano, Alaska. Journal of Geophysical Research: Solid Earth, 117(B2).

Medina-Martínez, F., Espíndola, J.M., De la Fuente, M., Mena, M., 1996. A gravity model of the Colima, México region. Geofis. Int. 35(4), 409–414.

Michaeli, W., 1991. Extrusionswerkzeuge für Kunststoffe und Kautschuk: Bauarten, Gestaltung und Berechnungsmöglichkeiten. Hanser Verlag.

Moeck, I., Schandelmeier, H. and Holl, H.G., 2009. The stress regime in a Rotliegend reservoir of the Northeast German Basin. Int. J. Earth. Sci. 98, 1643-1654.

Mutter, J.C., Carbotte, S.M., Su, W.S., Xu, L.Q., Buhl, P., Detrick, R.S., Kent, G.M., Orcutt, J.A., Harding, A.J., 1995. Seismic images of active magma systems beneath the East Pacific Rise between 17-degrees-05's and 17-degrees-35's. Science 268, 391–395.

Newman, A. V., Dixon, T. H., Ofoegbu, G. I., and Dixon, J. E., 2001. Geodetic and seismic constraints on recent activity at Long Valley Caldera, California: evidence for viscoelastic rheology. Journal of Volcanology and Geothermal Research, 105(3), 183-206.

Norini, G., Agliardi, F., Crosta, G., Groppelli, G., and Zuluaga, M.C., 2019. Structure of the Colima Volcanic Complex: Origin and Behaviour of Active Fault Systems in the Edifice. In Volcán de Colima (pp. 27-54). Springer, Berlin, Heidelberg.

Norini G, Capra L, Groppelli G, Agliardi F, Pola A, Cortes A., 2010. Structural architecture of the Colima Volcanic Complex. J Geophys Res 115, B12209.

Núnez-Cornú F, Nava FA, De la Cruz-Reyna S, Jiménez Z, Valencia C, García-Arthur R., 1994. Seismic activity related to the 1991 eruption of Colima Volcano, Mexico. Bull Volcanol 56: 228–237.

Parfitt, E. A., and L. Wilson, 2008. "The role of volatiles." Fundamentals of Physical Volcanology, 64-76.

Pinel, V., and Jaupart, C., 2004. Magma storage and horizontal dyke injection beneath a volcanic edifice. Earth and Planetary Science Letters, 221(1-4), 245-262.

Pinel, V., Carrara, A., Maccaferri, F., Rivalta, E., and Corbi, F., 2017. A two-step model for dynamical dike propagation in two dimensions: Application to the July 2001 Etna eruption. Journal of Geophysical Research: Solid Earth, 122(2), 1107-1125.

Pritchard, M. E., and Simons, M., 2004. An InSAR-based survey of volcanic deformation in the central Andes. Geochemistry, Geophysics, Geosystems, 5(2).

Rao SS., 1989. The Finite Element Method in Engineering second edition. PERGAMON PRESS 1989 ISBN 0-08-033419-9.

Rao, S.S., 2013. The Finite Element Method in Engineering: Pergamon International Library of Science, Technology, Engineering and Social Studies. Elsevier.

Reubi, O., Blundy, J., and Varley, N.R., 2013. Volatiles contents, degassing and crystallisation of intermediate magmas at Volcan de Colima, Mexico, inferred from melt inclusions. Contributions to Mineralogy and Petrology, 165(6), 1087-1106.

Reubi, O., Blundy, J., and Pickles, J., 2019. Petrological monitoring of Volcán de Colima magmatic system: the 1998 to 2011 activity. In Volcán de Colima (pp. 219-240). Springer, Berlin, Heidelberg.

Rivalta et al., 2019. Stress inversions to forecast magma pathways and eruptive vent location Sci. Adv. 2019; 5:eaau9784 .

Rivalta, E., Corbi, F., Passarelli, L., Acocella, V., Davis, T., and Di Vito, M.A., 2019. Stress inversions to forecast magma pathways and eruptive vent location. Science advances, 5(7), eaau9784.

Robin, C., Mossand, P., Camus, G., Cantagrel, J. M., Gourgaud, A., and Vincent, P.M., 1987. Eruptive history of the Colima volcanic complex (Mexico). Journal of Volcanology and Geothermal Research, 31(1-2), 99-113.

Ronchin, E., Masterlark, T., Molist, J. M., Saunders, S., and Tao, W., 2013. Solid modeling techniques to build 3D finite element models of volcanic systems: an example from the Rabaul Caldera system, Papua New Guinea. Computers & Geosciences, 52, 325-333.

Ronchin, E., Geyer, A., and Martí, J., 2015. Evaluating topographic effects on ground deformation: insights from finite element modeling. Surveys in Geophysics, 36(4), 513-548.

Rosas-Elguera, J., Ferrari, L., Garduño-Monroy, V.H., Urrutia-Fucugauchi, J., 1996: Continental boundaries of the Jalisco block and their influence in the Pliocene-Quaternary kinematics of western Mexico. Geology 24, 921–924.

Rosas-Elguera J, Ferrari L, Martinez ML, Urrutia-Fucugauchi J., 1997. Stratigraphy and tectonics of the Guadalajara region and triple- junction area, western Mexico. Int Geol Rev 39:125–140. doi:10.1080/00206819709465263.

Rosas-Elguera, J., Alva-Valdivia, L. M., Goguitchaichvili, A., Urrutia-Fucugauchi, J., Ortega-Rivera, M. A., Prieto, J.C.S., and Lee, J.K., 2003. Counterclockwise rotation of the Michoacan Block: implications for the tectonics of western Mexico. International Geology Review,45(9), 814-826.

Roverato, M., Capra, L., Sulpizio, R., Norini, G., 2011. Stratigraphic reconstruction of two debris avalanche deposits at Colima Volcano (Mexico): insights into pre-failure conditions and climate influence. Journal of Volcanology and Geothermal Research, 207(1-2), 33-46, 2011

Roverato, M., and Capra, L., 2013. Características microtexturales como indicadores del transporte y emplazamiento de dos depósitos de avalancha de escombros del Volcán de Colima (México). Revista mexicana de ciencias geológicas, 30(3), 512-525.

Salzer J.T., Nikkhoo M., Walter T., Sudhaus H., Reyes-Dàvila G., Bretòn-Gonzalez M., Aràmbula R., 2014. Satellite radar data reveal short-term pre-explosive displacements and a complex conduit system at Volcan de Colima, Mexico. Front Earth Sci 2:12.

Saada, A.S., 2009. Elasticity: Theory and Applications. Krieger, Malabar, Florida.

Savin, G. N., 1961. Stress concentration around holes.

Saucedo R, Macías J., Gavilanes JC, Arce JL, Komorowski JC, Gardner JE, Valdez-Moreno G., 2010. Eyewitness, stratigraphy, chemistry, and eruptive dynamics of the 1913 Plinian eruption of Volcán de Colima. México. J Volcanol Geotherm Res 191:149–166.

Saucedo R, Macìas JL, Gavilanes JC, Arce JL, Komorowski JC, Gardner JE, and Valdez-Moreno G., 2011. Corrigendum to Eyewitness, stratigraphy, chemistry, and eruptive dynamics of the 1913 plinian eruption of Volcan de Colima, Mexico. J Volcanol Geotherm Res 191:149–166.

Schwarz, H.R., 1991. Methode der finiten Elemente neubearbeitete Auflage, B.G. Teubner Stuttgart ISBN 3-519-22349-X.

Selvans, M. M., Stock, J. M., DeMets, C., Sanchez, O., and Marquez-Azua, B., 2011. Constraints on Jalisco Block motion and tectonics of the Guadalajara triple junction from 1998–2001 Campaign GPS Data. Pure and applied geophysics, 168(8-9), 1435-1447.

Serpa, L., Smith, S., Katz, C., Skidmore, C., Sloan, R., Pavlis, T., 1992. A geophysical investigation of the southern Jalisco block in the state of Colima, Mexico. Geofisica Internacional 31, 247–252.

Simms MA., and Graven G., 2004. Thermal convection in faulted extensional sedimentary basins: theoretical results from finite-element modelling. Geofluids (2004), 4, 109-130.

Singh, S. C., Crawford, W. C., Carton, H., Seher, T., Combier, V., Cannat, M., and Miranda, J. M., 2006. Discovery of a magma chamber and faults beneath a Mid-Atlantic Ridge hydrothermal field. Nature, 442(7106), 1029.

Sinton, J.M., and Detrick, R.S., 1992. Mid-ocean ridge magma chambers. Journal of Geophysical Research: Solid Earth, 97(B1), 197-216.

Stock JM and Lee J., 1994. Do microplates in subduction zones leave a geological record? Tectonics 13:1472–1487.

Stoopes, G. R., and Sheridan, M.F., 1992. Giant debris avalanches from the Colima Volcanic Complex, Mexico: Implications for long-runout landslides (> 100 km) and hazard assessment. Geology, 20(4), 299-302.

Spica, Z., Cruz-Atienza, V.M., Reyes-Alfaro, G., Legrand, D., and Iglesias, A., 2014. Crustal imaging of western Michoacán and the Jalisco Block, Mexico, from ambient seismic noise. Journal of Volcanology and Geothermal Research, 289, 193-201.

Spica Z, Perton M, Legrand D., 2017. Anatomy of the Colima volcano magmatic system, Mexico, Earth Planet Sci Lett 459: 1-13.

Suárez, G., Garcia-Acosta, V., Gaulon, R., 1994. Active crustal deformation in the Jalisco block, Mexico: evidence for a great historical earthquake in the 16th century. Tectonophysics 234, 117–12.

Sulpizio, R., Lucchi, F., Forni, F., Massaro, S., and Tranne, C., 2016. Unravelling the effusive-explosive transitions and the construction of a volcanic cone from geological data: The example of Monte dei Porri, Salina Island (Italy). Journal of Volcanology and Geothermal Research, 327, 1-22.

Sulpizio, R., and Massaro, S., 2017. Influence of stress field changes on eruption initiation and dynamics: a review. Frontiers in Earth Science, 5, 18.

Tibaldi, A., 2015. Structure of volcano plumbing systems: A review of multi-parametric effects. Journal of Volcanology and Geothermal Research 298 (2015) 85–135.

Touloukian, Y.S., Judd, W.R., Roy, R.F., 1989. Physical Properties of Rocks and Minerals, vol. 548. Hemisphere, New York.

Turcotte, D. L. and Schubert, G., 2002. Geodynamics, 2nd edition, Cambridge University Press.

Zehner B, Jana H. Börner J.H., Görz I., Spitzer K., 2015. Workflows for generating tetrahedral meshes for finite element simulations on complex geological structures. Computers and Geosciences, 79, 105-117.

Zhao, S., Muller, R. D., Takahashi, Y. and Kaneda, Y., 2004. 3-D finite-element modelling of deformation and stress associated with faulting: effect of inhomogeneous crustal structures, Geophys. J. Int., 157, 629– 644.

Zhong, X. Marcin, Dabrowski, Bjørn Jamtveit, 2019. Analytical solution for the stress field in elastic half space with a spherical pressurized cavity or inclusion containing eigenstrain. Geophysical Journal International · (submitted).

Zobin, V.M., Luhr, J.F., Taran, Y.A., Bretón, M., Cortés,A., De la Cruz-Reyna, S., Domínguez, T., Galindo, I., Gavilanes, J.C., Muñiz, J.J., Navarro, C., Ramírez, J. J., Reyes, G.A., Ursúa, M., Velasco, J., Alatorre, E., Santiago, H., 2002. Overview of the 1997–2000 activity of Volcán de Colima, Mexico. J. Volcanol. Geotherm.Res. 117, 1–19.

Watanabe, T., Masuyama, T., Nagaoka, K., Tahara, T., 2002. Analog experiments on magma-filled cracks: competition between external stresses and internal pressure. Earth Planets Space 54, 1247–1261.

Wang, R., Martin, F.L. and Roth, F., 2003. Computation of deformation induced by earthquakes in a multi-layered elastic crust-FORTRAN programs EDGRN/EDCMP, Comput. Geosci., 29, 195–207.

Eyewitness, stratigraphy, chemistry, and eruptive dynamics of the 1913 plinian eruption of Volcan de Colima, Mexico. J Volcanol Geotherm Res 191:149–166.

Schwarz, H.R., 1991. Methode der finiten Elemente neubearbeitete Auflage, B.G. Teubner Stuttgart ISBN 3-519-22349-X.

Selvans, M. M., Stock, J. M., DeMets, C., Sanchez, O., and Marquez-Azua, B., 2011. Constraints on Jalisco Block motion and tectonics of the Guadalajara triple junction from 1998–2001 Campaign GPS Data. Pure and applied geophysics, 168(8-9), 1435-1447.

Serpa, L., Smith, S., Katz, C., Skidmore, C., Sloan, R., Pavlis, T., 1992. A geophysical investigation of the southern Jalisco block in the state of Colima, Mexico. Geofisica Internacional 31, 247–252.

Simms MA., and Graven G., 2004. Thermal convection in faulted extensional sedimentary basins: theoretical results from finite-element modelling. Geofluids (2004), 4, 109-130.

Singh, S. C., Crawford, W. C., Carton, H., Seher, T., Combier, V., Cannat, M., and Miranda, J. M., 2006. Discovery of a magma chamber and faults beneath a Mid-Atlantic Ridge hydrothermal field. Nature, 442(7106), 1029.

Sinton, J.M., and Detrick, R.S., 1992. Mid-ocean ridge magma chambers. Journal of Geophysical Research: Solid Earth, 97(B1), 197-216.

Stock JM and Lee J., 1994. Do microplates in subduction zones leave a geological record? Tectonics 13:1472–1487.

Stoopes, G. R., and Sheridan, M.F., 1992. Giant debris avalanches from the Colima Volcanic Complex, Mexico: Implications for long-runout landslides (> 100 km) and hazard assessment. Geology, 20(4), 299-302.

Spica, Z., Cruz-Atienza, V.M., Reyes-Alfaro, G., Legrand, D., and Iglesias, A., 2014. Crustal imaging of western Michoacán and the Jalisco Block, Mexico, from ambient seismic noise. Journal of Volcanology and Geothermal Research, 289, 193-201.

Spica Z, Perton M, Legrand D., 2017. Anatomy of the Colima volcano magmatic system, Mexico, Earth Planet Sci Lett 459: 1-13.

Suárez, G., Garcia-Acosta, V., Gaulon, R., 1994. Active crustal deformation in the Jalisco block, Mexico: evidence for a great historical earthquake in the 16th century. Tectonophysics 234, 117–12.

Sulpizio, R., Lucchi, F., Forni, F., Massaro, S., and Tranne, C., 2016. Unravelling the effusive-explosive transitions and the construction of a volcanic cone from geological data: The example of Monte dei Porri, Salina Island (Italy). Journal of Volcanology and Geothermal Research, 327, 1-22.

Sulpizio, R., and Massaro, S., 2017. Influence of stress field changes on eruption initiation and dynamics: a review. Frontiers in Earth Science, 5, 18.

Tibaldi, A., 2015. Structure of volcano plumbing systems: A review of multi-parametric effects. Journal of Volcanology and Geothermal Research 298 (2015) 85–135.

Touloukian, Y.S., Judd, W.R., Roy, R.F., 1989. Physical Properties of Rocks and Minerals, vol. 548. Hemisphere, New York.

Turcotte, D. L. and Schubert, G., 2002. Geodynamics, 2nd edition, Cambridge University Press.

Zehner B, Jana H. Börner J.H., Görz I., Spitzer K., 2015. Workflows for generating tetrahedral meshes for finite element simulations on complex geological structures. Computers and Geosciences, 79, 105-117.

Zhao, S., Muller, R. D., Takahashi, Y. and Kaneda, Y., 2004. 3-D finite-element modelling of deformation and stress associated with faulting: effect of inhomogeneous crustal structures, Geophys. J. Int., 157, 629– 644.

Zhong, X. Marcin, Dabrowski, Bjørn Jamtveit, 2019. Analytical solution for the stress field in elastic half space with a spherical pressurized cavity or inclusion containing eigenstrain. Geophysical Journal International · (submitted).

Zobin, V.M., Luhr, J.F., Taran, Y.A., Bretón, M., Cortés,A., De la Cruz-Reyna, S., Domínguez, T., Galindo, I., Gavilanes, J.C., Muñiz, J.J., Navarro, C., Ramírez, J. J., Reyes, G.A., Ursúa, M., Velasco, J., Alatorre, E., Santiago, H., 2002. Overview of the 1997–2000 activity of Volcán de Colima, Mexico. J. Volcanol. Geotherm.Res. 117, 1–19.

Watanabe, T., Masuyama, T., Nagaoka, K., Tahara, T., 2002. Analog experiments on magma-filled cracks: competition between external stresses and internal pressure. Earth Planets Space 54, 1247–1261.

Wang, R., Martin, F.L. and Roth, F., 2003. Computation of deformation induced by earthquakes in a multi-layered elastic crust-FORTRAN programs EDGRN/EDCMP, Comput. Geosci., 29, 195–207.